Article

Multifunctional HNT@Fe₃O₄@PPy@DOX Nanoplatform for Effective Chemo-Photothermal Combination Therapy of Breast Cancer with MR Imaging

Xiang Luo,[†] Jun Zhang,[†] Yan-Ping Wu,[†] Xiaohan Yang, Xiu-Ping Kuang, Wei-Xi Li, Yi-Fang Li, Rong-Rong He,* and Mingxian Liu*

Read Online

ACCESS | Metrics & More | Article Recommendations | SI Supporting Information

ABSTRACT: Multifunctional nanoparticles for imaging and treatment in cancer are getting more and more attention recently. Herein, halloysite nanotubes (HNTs), natural clay nanotubes, are designed as multifunctional nanoplatform for targeted delivering photothermal therapy agents and chemotherapeutic drugs. Fe_3O_4 was anchored on the outer surfaces of HNTs and then doxorubicin (DOX) was loaded on the nanotubes. Afterward, a layer of polypyrrole (PPy), as photothermal agent, was wrapped on the tubes. The nanoplatform of HNT@Fe₃O₄@PPy@DOX can be guided to tumor tissue by an external magnetic field, and then performs chemo-photothermal combined therapy by 808 nm laser irradiation. HNT@Fe₃O₄@PPy@DOX shows the ability of T_2-weighted magnetic resonance imaging, which could be considered as a promising application in magnetic targeting tumor therapy. In vitro and in vivo experiments demonstrate that HNTs nanoplatform has good biocompatibility and produces a strong antitumor effect trigged by near-infrared laser irradiation. The novel chemo-photothermal therapy nanoplatform based on HNTs may be developed as a multifunctional nanoparticle for imaging and therapy in breast cancer.

KEYWORDS: *halloysite nanotubes, polypyrrole, chemo-photothermal therapy, magnetic targeted, breast cancer*
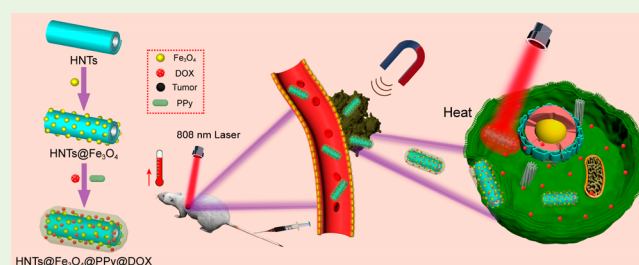
1. INTRODUCTION

Photothermal therapy (PTT) is an effective treatment in cancer that converts near-infrared (NIR) light energy into heat through a photothermal agent, which leads to a rapid increase of temperature in tumor sites.[1] More and more evidence from reported research reveals that cancer cells are more sensitive to PTT than normal cells.[2,3] PTT has the advantages of high temporal and spatial resolution, safety, high efficiency, and noninvasiveness.[4,5] However, PTT cannot completely inhibit tumor growth because of the uneven heat distribution and heat resistance during irradiation.[6,7] In order to achieve better therapeutic effects toward tumor, researchers have extensively studied combinations with photodynamic therapy,[8,9] chemo-therapy,[10,11] gene therapy,[12,13] or immunotherapy.[14] In these methods, nanomaterial platform designed with the combination of diagnosis and therapy is significant because the nanomaterials can amplify the anticancer efficiency.[12,15]

Up to now, a variety of photothermal therapeutic agents have been studied. For example, inorganic or metal materials including gold nanomaterials,[16−18] carbon nanomaterials,[19,20] iron oxide,[21−23] and metal sulfide nanoparticles[24,25] show a high photothermal conversion effect. Organic materials including polypyrrole (PPy),[26] polydopamine,[27] and phthalo-cyanine[28] are also easily synthesized and show satisfied

photothermal therapy effect. Among them, PPy is widely applied in organic electronic products because of its high electrical conductivity and excellent stability.[29] In addition, PPy wrapping can stabilize the dispersion of nanoparticles in biological environment. Iron oxide (Fe_3O_4) shows great potentials in biomedical areas, because of its good biocompatibility, high light-to-heat conversion efficiency, and excellent targeted drug delivery.[21,23,30] Therefore, the combination of PPy with Fe_3O_4 can contribute an excellent magnetic targeted PTT system and provide an effective cancer therapeutic nanoplatform.

Halloysite nanotubes (HNTs) are novel one-dimensional nanomaterials that have many advantages such as unique hollow lumen structure, high adsorption capacity, ease of functionalization, high biocompatibility, and biosafety.[31−33] The length of the natural nanotubes ranges from 200 to 1500 nm, whereas the outer diameter of HNTs is in 30−70 nm.[34]

HNTs can be loaded with different drugs and protect the drug from decomposition, prolong the drug release period, and decrease the side effects of drugs. HNTs can also act as gene vectors to achieve cancer treatment. For examples, curcumin loaded in chitosan-grafted HNTs produces higher reactive oxygen species (ROS),[32] and polyamide-grafted HNTs can deliver siRNA intracellularly.[35] It is believed that rod-shaped particles have obvious advantages in cell internalization rate and intracellular trafficking compared to spherical, cylindrical, and cubic particles.[36] Meanwhile, Fe_3O_4@HNTs shows no hysteresis and superparamagnetic behavior.[37,38] Therefore, HNTs decorated with Fe_3O_4, PPy, and chemotherapy drugs may produce a multifunctional nanoplatform with integrated imaging and treatment, good dispersion ability overcoming the aggregation of PPy, and preferably phagocytic efficiency of cells.

In this study, HNT@Fe_3O_4@PPy was prepared by anchoring of Fe_3O_4 on the surfaces of HNTs, then wrapping with a layer of PPy and loading with chemotherapeutic drug (doxorubicin, DOX). The HNT@Fe_3O_4@PPy@DOX nanoplatform can be guided to the tumor by the action of an external magnet, and the chemo-photothermal therapy of the tumor can be achieved by laser irradiation. Meanwhile, both Fe_3O_4 and PPy have strong photothermal conversion effects. In vitro and in vivo experiments demonstrated that the nanoplatform could be targeted to the tumor sites and produce a temperature increase by laser irradiation to kill the tumor cells. The construction of the HNT@Fe_3O_4@PPy@DOX therapeutic nanoplatform provided an effective, biocompatible, and cheap choice for clinical targeting therapy toward breast cancer.

2. EXPERIMENTAL SECTION

2.1. Materials. Purified HNTs were acquired by Guangzhou Runwo Materials Technology Co., Ltd., China. $FeSO_4 \cdot 7H_2O$ (99.8%), $FeCl_3 \cdot 6H_2O$ (99.8%), and $NH_3 \cdot H_2O$ (25%) were obtained from Guangzhou Chemical Reagent Factory. Pyrrole (99.5%) was purchased from Sigma-Aldrich Trading Co., Ltd., China. Poly(vinyl alcohol) (PVA, 99%) was purchased from China Petrochemical Group Co., Ltd., China. DOX was purchased from Nanjing Oddfoni Biological Technology Co., Ltd., China. Cell Counting Kit-8 (CCK-8) reagents were purchased from BestBio Biology Co., Ltd., China. Acridine orange (AO) and ethidium bromide (EB) were purchased from Solarbio Science & Technology Co., Ltd., China. Ultrapure water was prepared using a Milli-Q Integral Water Purification System. Other chemicals were of analytical grade and used as received without further purification.

2.2. Synthesis of HNT@Fe_3O_4 Nanocomposites. HNT@Fe_3O_4 was prepared according to the reported method.[39] HNTs (0.5 g) were dispersed in 200 mL of ultrapure water by ultrasound (20 kHz, 20 min). Then, $FeCl_3 \cdot 6H_2O$ (1.165 g) (as oxidizing agent) and $FeSO_4 \cdot 7H_2O$ (0.48 g) were added to the dispersion under magnetic stirring at 60 °C. The $NH_3 \cdot H_2O$ (10 mL) solution was added dropwise to prepare Fe_3O_4. The pH of final mixture was controlled to be in the range of 9−10. The mixture was then heated to 70 °C for 4 h, washed three times with distilled water, and finally dried at 60 °C for 3 h.

2.3. Synthesis of HNT@Fe_3O_4@PPy@DOX Nanocomposites. HNT@Fe_3O_4@PPy@DOX was prepared by the reported method.[40,41] PVA (5 g) was dissolved in 100 mL of ultrapure water at 85 °C, and HNT@Fe_3O_4 (0.7 g) was dispersed in 100 mL of ultrapure water and ultrasonically dispersed. PPy was synthesized via a facile one-step aqueous dispersion polymerization using PVA as a stabilizer. After cooling the PVA aqueous solution to room temperature, the aqueous dispersion of HNT@Fe_3O_4 was added and stirred for 30 min. DOX (30 mg) and $FeCl_3 \cdot 6H_2O$ (6.3 g) were then added to the mixture and stirred for 1 h. Additionally, Py monomer (1.4 mL) was

added and stirred at room temperature for 24 h in the dark. The obtained black product was washed several times with deionized water and centrifuged, and then freeze-dried to obtain a product. The adsorption of DOX was calculated at 480 nm using an ultraviolet spectrophotometer. The DOX loading efficiency was calculated by the DOX standard curve to be 2.3%. The loading efficiency was calculated as follows.

$$\text{loading efficiency}(\%) = \frac{\text{weight of loaded DOX}}{\text{total weight of nanoparticles and loaded DOX}} \times 100\%$$

2.4. Characterization of HNT@Fe_3O_4@PPy@DOX. An aqueous dispersion of all samples (concentration of 0.05%) was dropped onto a copper network with a carbon support film and observed using a transmission electron microscope (TEM, JEM2100F, JEOL Ltd., Japan) at an accelerating voltage of 100 kV. The UV−visible spectrophotometers of all samples were measured by a UV−visible spectrometer (UV-2550, Shimadzu Instrument Ltd., China). The crystal structure was analyzed by X-ray diffraction (XRD, MiniFlex-600, Rigaku Corporation, Japan). The element content was analyzed by X-ray photoelectron spectroscopy (XPS, ESCALAB250Xi, Thermo Fisher Scientific Ltd., USA). Infrared photograph and temperature elevation recordings were captured by a photothermal imaging system (TiS 55, Fluke Electronic Instrument Ltd., USA) using an 808 nm fiber-coupled laser as a light source (MD-III-808, Changchun New Industry Optoelectronic Technology Ltd., China). Cell apoptosis and necrosis were tested by flow cytometry (BD FACSCanto, USA). Fluorescent images of the cells were taken by laser scanning confocal microscopy (LSCM, LSM880, Carl Zeiss AG, Germany). The MR imaging was obtained by a magnetic resonance imaging system (M3, Aspect Imaging Ltd., Israel). The zeta potential test was measured at 25 °C using NanoBrook Omni (Brook Haven Instrument Co., Ltd., USA) at pH 7.4 (PBS buffer solution). The biodistribution images of HNT@Fe_3O_4@PPy@DOX in 4T1-bearing mice were determined by an in vivo fluorescence imaging system (In-Vivo FX PRO, Bruker, USA).

2.5. In Vitro Photothermal Performance of HNT@Fe_3O_4@PPy@DOX. One milliliter of HNT@Fe_3O_4@PPy@DOX aqueous dispersion (500, 1000, and 2000 μg/mL) was added to a 1.5 mL EP tube, and then irradiated with 808 nm laser (0.8, 1, and 1.2 W/cm^2) for 8 min. Once the irradiation started, the temperature of the dispersion was recorded with an infrared camera every 1 min while taking an infrared photograph every 2 min. Each sample was repeated three times to calculate the mean value and standard error. Pure water as a control was treated under the same measurement conditions.

2.6. In Vitro Release of DOX. The PBS dispersion (5 mL) of HNT@Fe_3O_4@PPy@DOX (10 mg) was placed in a centrifuge tube and continuously shaken at 37 °C in the dark. A set of samples was irradiated with a laser (808 nm, 1 W/cm^2) for 8 min prior to sampling. After centrifugation (10 000 rpm, 2 min) at specific times, the supernatant (1.5 mL) of DOX release from HNT@Fe_3O_4@PPy@DOX was measured by UV−vis. The same volume of fresh PBS was then added to the tube.

2.7. Fe Content of HNT@Fe_3O_4@PPy@DOX. HNT@Fe_3O_4@PPy@DOX (15 mg) was mixed with 10 mL of aqua regia for digestion. After 12 h, the acidity of the mixture was adjusted to 0.1−1 mol/L. The test was then carried out using an inductively coupled plasma spectrometer (iCAP 7000 SERIES, Thermo Fisher Scientific Ltd., USA).

2.8. Cell Culture. Human normal breast cells (MCF10A), human breast cancer cells (MCF-7), and mouse breast cancer cells (4T1) were obtained from the cell bank of the Chinese Academy of Sciences. MCF10A and MCF-7 cells were cultured in Dulbecco's modified Eagle's medium (DMEM) (Gibco, USA), and 4T1 cells were maintained in RPMI 1640 (Gibco, USA) containing 10% fetal bovine serum (Gibco, USA). The culture was carried out under the conditions of a temperature of 37 °C and 5% CO_2.

2.9. In Vitro Cytotoxicity Study. MCF-7 cells (1 × 10^4 cells/well) were seeded in 96-well cell culture plates for 24 h, and then
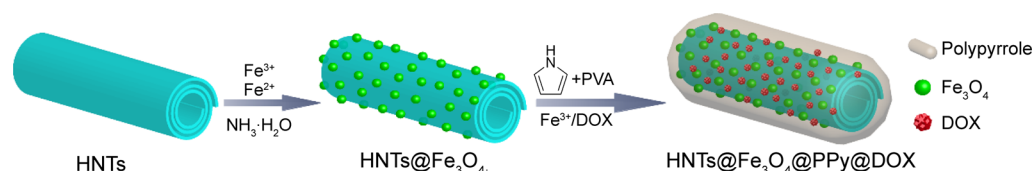
Figure 1. Schematic diagram of synthesizing HNT@Fe$_3$O$_4$@PPy@DOX.

cocultured with HNTs and HNT@Fe$_3$O$_4$@PPy (0, 31.25, 62.5, 125, 250, 500, and 1000 μg/mL) for 24 h at 37 °C. The cells were then washed twice with PBS and 100 μL of fresh medium was added. Last, 10 μL of CCK-8 reagent was added to each well and incubated for 4 h. The supernatant was centrifuged at 15 000 rpm to eliminate the effect of the materials on the absorbance results. MCF-7 cells were incubated for 24 h and then irradiated with or without an 808 nm laser (1 W/cm^2) for 8 min. After washing with PBS, 100 μL of the culture solution was added, and 10 μL of CCK-8 reagent was added to each well and incubated for 4 h. The supernatant was centrifuged at 15 000 rpm and the absorbance was recorded at 450 nm by a microplate reader.

2.10. AO/EB Staining Assay. MCF-7 cells (8 × 10^3 cells/well) were seeded in 96-well plates for 24 h, and then HNTs and HNT@Fe$_3$O$_4$@PPy@DOX (400 μg/mL) were added to each well to culture for 24 h. It was then irradiated with an 808 nm laser (1 W/cm^2) for 8 min. Finally, the cells were stained with AO/EB double fluorescent dye, washed three times with PBS, and observed in a fluorescence microscope.

2.11. Cell Apoptosis Assay. MCF-7 cells were seeded in 12-well plates at a density of 5 × 10^4 cells/well. After 24 h of incubation, HNTs and HNT@Fe$_3$O$_4$@PPy@DOX (400 μg/mL) were added to each well. The cells were then irradiated for 8 min with 808 nm laser (0.8 W/cm^2) in fresh DMEM medium at 37 °C. Untreated cells were tested as a negative control. All cells were then washed three times with PBS, trypsinized (EDTA), and collected by centrifugation. The cells were resuspended in 0.5 mL annexin buffer. All cells were then stained with propidium iodide (PI) and annexin V-FITC containing binding buffer for 15 min and finally detected by flow cytometry.

2.12. Fluorescent Staining of Cells. LSCM was used to observe the enrichment of HNT@Fe$_3$O$_4$@PPy@DOX at MCF-7 cells. MCF-7 cells (1 × 10^4 cells) were usually cultured in a Petri dish and allowed to adhere overnight in an atmosphere of 37 °C and 5% CO$_2$. The cells were then treated with HNT@Fe$_3$O$_4$@PPy@DOX (200 μg/mL) for 2, 4, and 8 h. The cells were washed three times with PBS, fixed with 4% paraformaldehyde for 15 min, and permeabilized with 0.1% Triton for 7 min. The nucleus was stained with 4′,6-diamidino-2-phenyl-indole (DAPI), and filamentous actin (F-actin) was stained with Alexa Fluor 488 phalloidin. The fluorescence images were observed by LSCM.

2.13. In Vivo Magnetic Targeted Efficiency and Fluorescence Imaging of HNT@Fe$_3$O$_4$@PPy@DOX. The pathogen-free BALB/c mice (∼20 g, female, 6−8 weeks old) were obtained from Guangdong Medical Laboratory Animal Center. All animal care and experiments were done following protocols approved by the Jinan University Laboratory Animal Center. To establish 4T1-bearing mice model in vivo, we transplanted 4T1 cells (2 × 10^6 cells/mL) in 200 μL of PBS into BALB/c mice by subcutaneous injection. Upon the tumor sizes reaching ∼100 mm^3, an 800G plate-shaped magnet with diameter of 8 mm and thickness of 2 mm was immobilized on the tumor area of each mouse using adhesive tape for 24 h after intravenously injected with DOX (0.52 mg/kg) and HNT@Fe$_3$O$_4$@PPy@DOX (0.52 mg DOX equiv/kg). The magnet was then removed before MR imaging or fluorescence imaging. The MR imaging was captured by an M3 Compact MRI System at indicated time points (0, 2, 4, 8, and 24 h). For fluorescence imaging, mice were sacrificed at indicated time points (0, 4, 8, and 24 h), and then tumors and major organs were obtained and observed through in vivo fluorescence imaging system. DOX was detected by fluorescence with excitation and emission wavelength at 480 and 550 nm, respectively.

2.14. In Vivo Photothermal Efficiency of HNT@Fe$_3$O$_4$@PPy@DOX. Upon the tumor sizes reaching ∼100 mm^3, an 800G plate-shaped magnet with diameter of 8 mm and thickness of 2 mm was immobilized on the tumor area of each mouse by using adhesive tape for 24 h after intravenously injected with with normal saline (300 μL) and HNT@Fe$_3$O$_4$@PPy@DOX (22.5 mg/kg). After 4 h injection, the tumor burden on 4T1-bearing mice were irradiated with 808 nm laser (1 W/cm^2, 8 min) according to the reported research with slight modifications.[42,43] Photothermal imaging was performed at scheduled time intervals (0, 2, 4, 6, and 8 min) by an infrared thermal camera and the temperature variation in tumor burden of the 4T1-bearing mice were monitored.

2.15. In Vivo Synergistic Chemo-Photothermal Therapeutic Efficiency of HNT@Fe$_3$O$_4$@PPy@DOX. Upon the tumor sizes reaching ∼100 mm^3, the 4T1-bearing mice were randomly allocated into five treatment groups, including a saline + laser group (300 μL of normal saline, i.v., and 1 W/cm^2 of laser irradiation, 8 min), HNT@Fe$_3$O$_4$@PPy group (22.5 mg/kg, i.v.), DOX group (0.52 mg/kg, i.v.), HNT@Fe$_3$O$_4$@PPy@DOX group (0.52 mg DOX equiv/kg, i.v.), and HNT@Fe$_3$O$_4$@PPy@DOX + laser group (0.52 mg DOX equiv/kg, i.v., and 1 W/cm^2 of laser irradiation, 8 min). An 800G plate-shaped magnet with diameter of 8 mm and thickness of 2 mm was immobilized on the tumor area of each mouse by using adhesive tape for 24 h after intravenous injection. After 4 h of administration, the tumor burden on 4T1-bearing mice were irradiated with 808 nm laser at a power density of 1 W/cm^2 maintained for 8 min. For the whole therapeutic period, the 4T1-bearing mice were treated with normal saline, HNT@Fe$_3$O$_4$@PPy, DOX, and HNT@Fe$_3$O$_4$@PPy@DOX every other day for 15 days and carried out irradiation 8 times. The body weight of each mouse was tracked every day, and the tumor volume of each mouse was measured every 3 days with a caliper and calculated according to the equation: tumor volume (mm^3) = 0.5 × [tumor length (mm)] × [tumor width (mm)]^2. The mice were euthanatized at the end of the experiment, and then the tumors, hearts, liver, spleen, lung, and kidneys of mice were obtained, washed with normal saline, and fixed in 4% paraformaldehyde.

2.16. In Vivo Hemocompatibility Assay of HNT@Fe$_3$O$_4$@PPy@DOX. BALB/c mice were randomized into two treatment groups: control group (300 μL of normal saline, i.v.) and HNT@Fe$_3$O$_4$@PPy@DOX group (22.5 mg/kg, i.v.). The mice were treated with 300 μL of normal saline or HNT@Fe$_3$O$_4$@PPy@DOX via intravenous injection every 3 days for 15 days. Blood samples were obtained from the orbital sinus. Blood smears were allowed to air-dry and stained with Wright-Giemsa (Nanjing Jiancheng Biotechnology Institute, China), and examined by a digital microscope and scanner (M8, Precipoint, Germany). Serum biochemistry was measured by Beckman Coulter AU680 analyzer (Beckman Coulter, Miami, FL, USA) and complete blood panel assay was detected by automatic biochemical analyzer (Sysmex-800, Sysmex Corporation, Kobe, Japan).

2.17. Histopathology Analysis. The fixed tissues (tumor, heart, liver, spleen, lung, and kidney) of mice were paraffined, cut into a thickness (4 μm) of the section and then stained with hematoxylin and eosin (H&E). For the detection of apoptosis-positive cells in tumor, terminal deoxyribonucleotidyl transferase (TDT)-mediated dUTP-digoxigenin nick end labeling (TUNEL) assay was performed according to manufacturer's instructions. Apoptosis positive cells were observed by a digital microscope and scanner (M8, Precipoint, Germany) and quantified in 5 randomly selected fields.
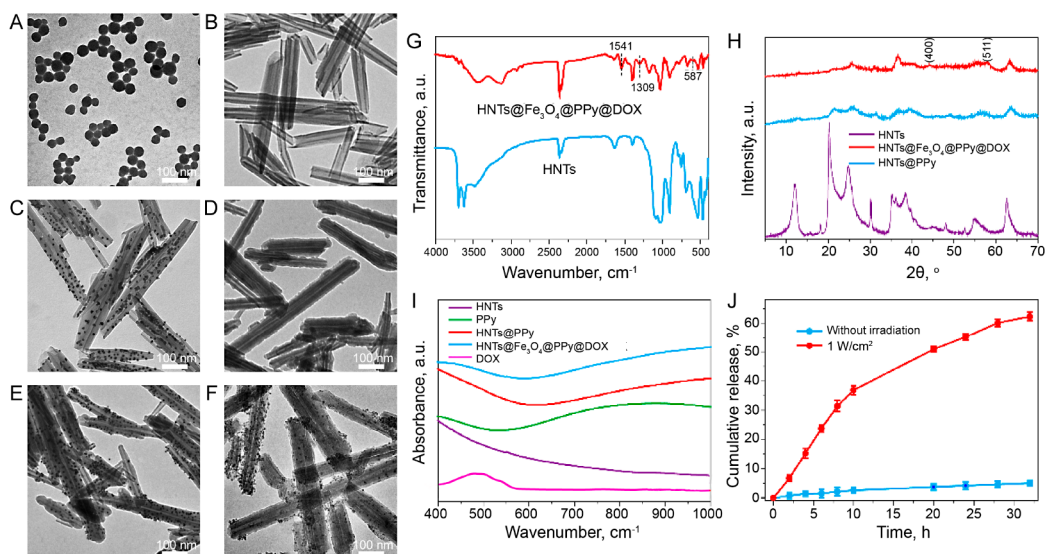
Figure 2. TEM images of (A) PPy nanospheres, (B) HNTs, (C) HNT@Fe$_3$O$_4$, (D) HNT@PPy, (E) HNT@Fe$_3$O$_4$@PPy, and (F) HNT@Fe$_3$O$_4$@PPy@DOX. (G) FTIR spectrum, (H) XRD patterns, and (I) ultraviolet absorption spectrum of different samples. (J) DOX release profile of HNT@Fe$_3$O$_4$@PPy@DOX with or without irradiation. The data showed mean ± SD ($n = 3$).

2.18. Statistical Analysis. Data are presented as means ± standard deviation (SD). Statistical comparisons of results were followed by GraphPad Prism 6 (GraphPad Software, USA). The DOX fluorescence in tumor tissues and the hemocompatibility of HNT@Fe$_3$O$_4$@PPy@DOX were analyzed by t-test. The data of body weight and tumor volume were analyzed using two-way ANOVA with Tukey's post hoc test. Magnetic tumor-targeted efficiency and temperature changes in tumor tissues, tumor weight, and apoptosis index were analyzed using one-way ANOVA with Tukey's post hoc test. Values of all significant correlations ($P < 0.05$) were considered statistically significant.

3. RESULTS AND DISCUSSIONS

3.1. Characterization of HNT@Fe$_3$O$_4$@PPy@DOX Nanocomposites. HNT@Fe$_3$O$_4$@PPy@DOX nanocomposites were synthesized by coprecipitation of Fe$_3$O$_4$ and PPy in the presence of HNTs (Figure 1). First, HNTs were uniformly dispersed in water by ultrasound (25 kHz, 20 min). FeCl$_3$·6H$_2$O and FeSO$_4$·7H$_2$O were added into the dispersion, and then NH$_3$·H$_2$O solution was added dropwise to prepare HNT@Fe$_3$O$_4$ by coprecipitation. Thereafter, HNT@Fe$_3$O$_4$ was dispersed in a solution of PVA. Last, DOX, FeCl$_3$·6H$_2$O and pyrrole were added to form a PPy layer-coated HNT@Fe$_3$O$_4$@PPy@DOX nanocomposites. Among them, Fe^{3+} was used as a catalyst to polymerize Py, and PVA was used as a stabilizer to help synthesize uniform PPy nanospheres.

HNT@Fe$_3$O$_4$@PPy@DOX shows strong magnetic properties. Under the action of the magnet, it can be adsorbed on the wall of the bottle to make the dispersion clear. In the absence of a magnet, the HNT@Fe$_3$O$_4$@PPy@DOX dispersion is stable (Figure S1). As shown in Figure S2, HNT@Fe$_3$O$_4$@PPy@DOX (1 mg/mL) was steadily dispersed in PBS at different temperatures (25, 37, 50, and 60 °C) after 4 h without agglomeration or sedimentation. The morphology of the prepared nanocomposites was further characterized by TEM. HNTs show rodlike morphology with tubular structure (Figure 2B). Py is polymerized to form a large number of nanospheres in absence of HNTs (Figure 2A). Fe$_3$O$_4$ nanoparticles can be firmly attached to the surfaces of the tubes and make nanomaterials magnetic (Figure 2C). After the addition of HNTs, Py is polymerized on the surface of HNTs

to form a layer of PPy (Figure 2D). It can be observed that HNT@Fe$_3$O$_4$@PPy@DOX has a large amount of Fe$_3$O$_4$ nanoparticles on the tubes' surface, and then the outermost layer is coated with a layer of PPy (Figure 2F). It is noted that HNT@Fe$_3$O$_4$@PPy@DOX has no obvious morphology change when compared with HNT@Fe$_3$O$_4$@PPy (Figure 2E). It can be explained by that DOX is loaded to nanotubes through physical adsorption.

The FTIR spectrum of HNT@Fe$_3$O$_4$@PPy@DOX shows that the characteristic peak at 1541 cm^{-1} is assigned to the tensile vibration of PPy ring, and the characteristic peak at 1309 cm^{-1} is assigned to C—N bond.[44] The characteristic peak at 587 cm^{-1} is the N—H deformation vibration peak (Figure 2G). XRD patterns show that the (400) and (511) planes related to Fe$_3$O$_4$ are not found in HNTs and HNT@PPy but appeared in HNT@Fe$_3$O$_4$@PPy@DOX. Also, the peak intensity of HNT@PPy and HNT@Fe$_3$O$_4$@PPy@DOX after PPy wrapping is significantly reduced (Figure 2H), which is caused by the PPy shielding effect in the surface of HNTs. These results preliminarily prove that Fe$_3$O$_4$ and PPy exist in HNT@Fe$_3$O$_4$@PPy@DOX. HNTs have no obvious absorption in the NIR region, but HNT@PPy has strong absorption in the entire NIR region. HNT@Fe$_3$O$_4$@PPy@DOX exhibits a weak absorption of DOX at 480 nm when compared to HNT@PPy (Figure 2I).

The DOX loading efficiency of HNT@Fe$_3$O$_4$@PPy@DOX is 2.3%, which was calculated by DOX standard curve. The release of DOX from nanocomposites in PBS is extremely low without irradiation, but greatly increased after laser irradiation (Figure 2J). The acceleration of desorption and release of DOX reveal that laser irradiation can promote the local temperature rising. The produced heating triggered the molecular desorption through the thermal movement of the carrier as well as the temperature-dependent molecular mobility of the drug.[45,46] These results demonstrate that DOX and Fe$_3$O$_4$ nanoparticles are successfully loaded on HNTs, with a layer of PPy.

The surface charge of HNTs is −27.1 mV, which explains that HNTs have good water (pH 7) dispersing ability for its high surface negative charge-induced repulsion effect. The
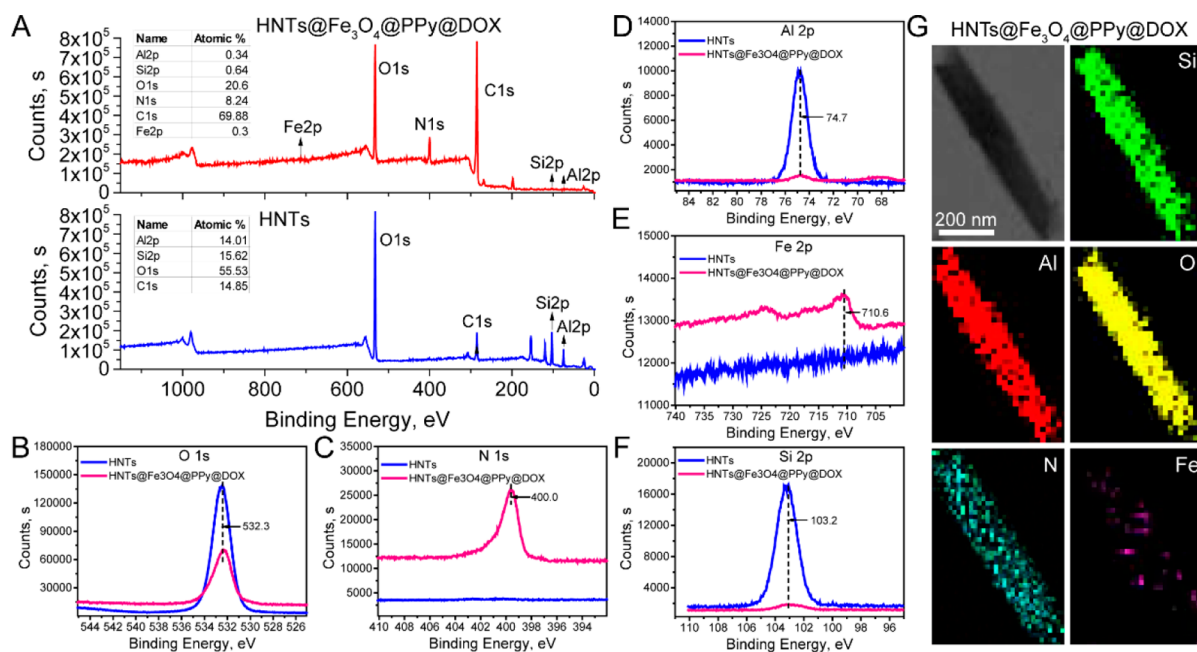
Figure 3. (A) XPS spectral curves for HNTs and HNT@Fe$_3$O$_4$@PPy@DOX. (B−F) High-resolution scanning of O, N, Al, Fe, and Si elements of HNT@Fe$_3$O$_4$@PPy@DOX. (G) Si, Al, O, N, and Fe element mapping corresponding to TEM images of HNT@Fe$_3$O$_4$@PPy@DOX.
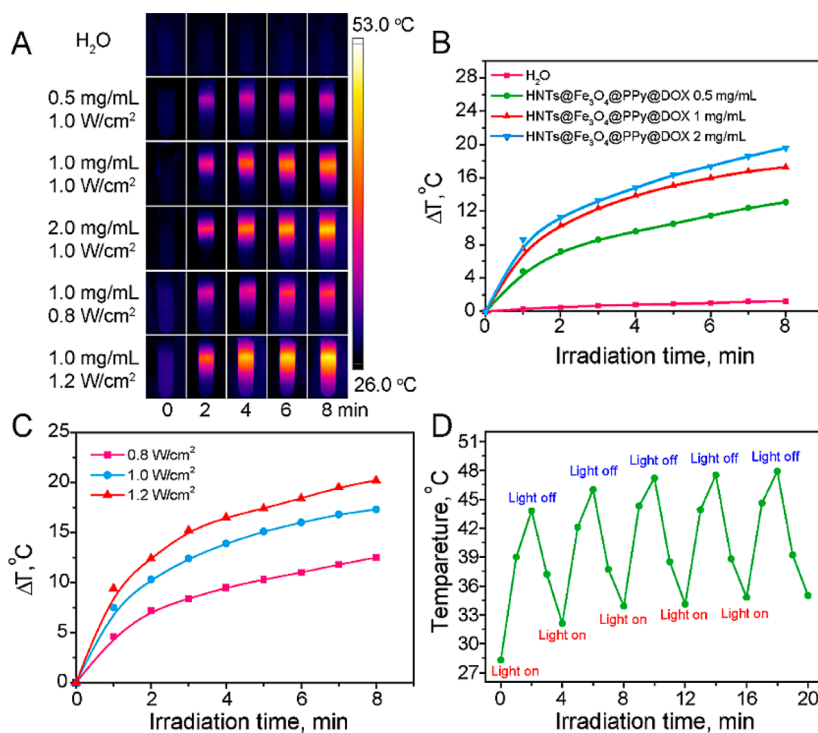

Figure 4. (A) Infrared images of HNT@Fe$_3$O$_4$@PPy@DOX dispersion in different concentrations and different powers under irradiation of 808 nm laser recorded using infrared camera. (B) Temperature curves of HNT@Fe$_3$O$_4$@PPy@DOX dispersion (1 mL) with different concentrations irradiated by 808 nm laser (1 W/cm^2). (C) Temperature curves of HNT@Fe$_3$O$_4$@PPy@DOX (1 mg/mL, 1 mL) upon NIR light irradiation with various powers. (D) Temperature curves of HNT@Fe$_3$O$_4$@PPy@DOX (1 mg/mL, 1 mL) with an 808 nm laser switch-on/-off five times. The data are represented as mean ± SD (n = 3).

surface charge of HNT@PPy is +24.5 mV, because PPy is a positively charged polymer. It is noted that there is no significant change in the surface charge of HNT@Fe$_3$O$_4$@PPy@DOX (+24.8 mV) while compared to HNT@PPy (Figure S3A). This phenomenon can be explained by DOX with a positive charge being encapsulated in the PPy layer. The

average particle size of HNTs, HNT@PPy and HNT@Fe$_3$O$_4$@PPy@DOX is 323.5 ± 13.8, 482.7 ± 11.6, and 501.7 ± 14.2 nm, respectively (Figure S3B, D). Compared with HNTs, the particle size of HNT@PPy and HNT@Fe$_3$O$_4$@PPy@DOX increased significantly, because of the wrapping of PPy on nanotubes.
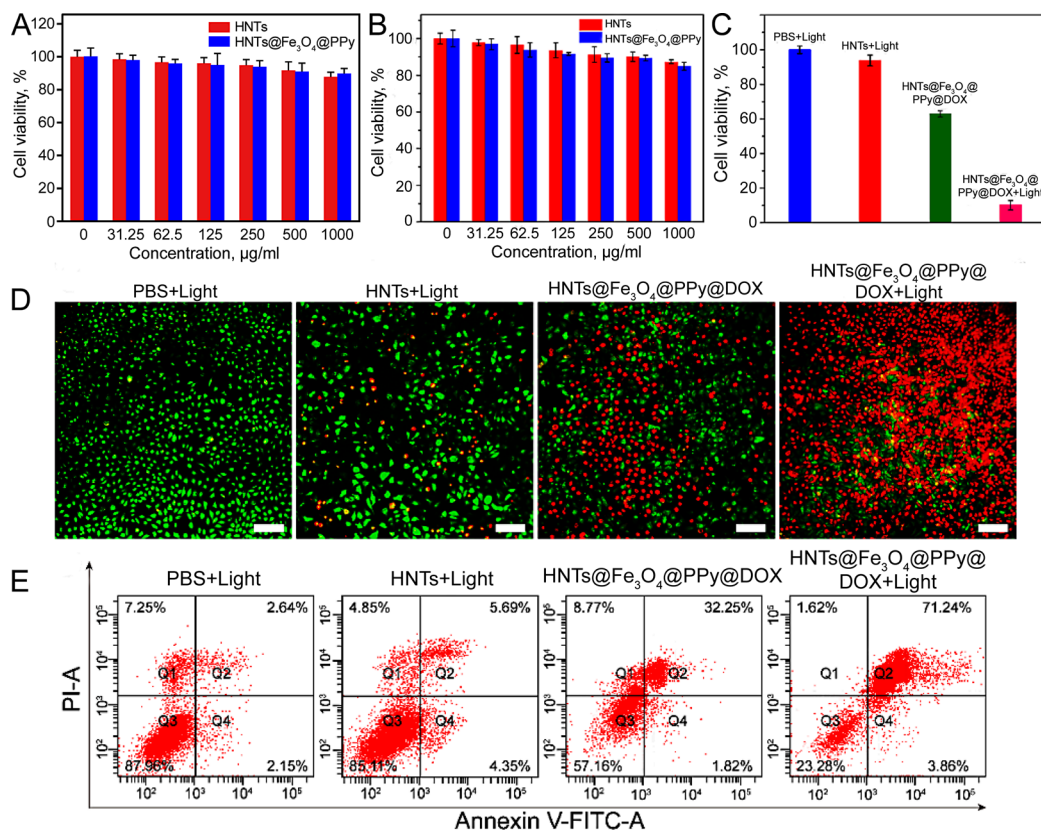
Figure 5. Relative survival of MCF10A (A) and MCF-7 (B) cells treated with different concentrations of HNTs and HNT@Fe$_3$O$_4$@PPy@DOX for 24 h. (C) Relative survival rate of MCF-7 cells incubated with HNTs and HNT@Fe$_3$O$_4$@PPy@DOX for 12 h and then with or without irradiation (808 nm, 1 W/cm^2) for 8 min. The data showed mean ± SD (n = 4). (D) Fluorescent images of MCF-7 cells incubated with HNTs and HNT@Fe$_3$O$_4$@PPy@DOX and treated with or without irradiation (808 nm, 1 W/cm^2) for 8 min. Color in green indicates live cells and color in red indicates dead cells. Scale bar: 50 μm. (E) Ratio of apoptosis in MCF-7 cells incubated with HNTs, DOX, and HNT@Fe$_3$O$_4$@PPy@DOX, with or without 808 nm laser irradiated (1 W/cm^2) for 8 min.

The composition of elements of HNTs and HNT@Fe$_3$O$_4$@PPy@DOX is further investigated by XPS. Results from XPS spectral curves show that the contents of N and Fe in HNT@Fe$_3$O$_4$@PPy@DOX are 8.24 and 0.3%, respectively, whereas those in HNTs are 0 (Figure 3A). It is suggested that HNTs are natural clay minerals with a small number of contaminants. The C content of modified HNTs increased from 14.85 to 69.88%, whereas the contents of O, Al, and Si elements decreased from 55.53 to 20.6%, 14.01 to 0.34%, and 15.62 to 0.64%, respectively (Figure 3A). This is because the PPy wrapping on the surface of HNTs increases the content of C and N elements and decreases the content of O, Al, and Si elements. Because the depth of the XPS test material is only in a few nanometers, only a low content of Fe is detected. To quantitatively analyze the content of Fe in the material, we conducted an ICP test and it was shown that Fe element content was 6.4% (weight ratio of Fe to HNT@Fe$_3$O$_4$@PPy@DOX). The high-resolution XPS scan curves for the O, N, Al, Fe, and Si elements in HNTs and HNT@Fe$_3$O$_4$@PPy@DOX are displayed in Figure 3B, F. Fe 2p and N 1s electrons were detected in HNT@Fe$_3$O$_4$@PPy@DOX but not in raw HNTs. The element mapping showed in TEM images further confirms that O, N, Al, Fe, and Si elements exist in HNT@Fe$_3$O$_4$@PPy@DOX (Figure 3G). These data demonstrate that the surface of HNTs is loaded with Fe$_3$O$_4$ nanoparticles and surrounded by a layer of PPy.

The temperature increase capabilities of ultrapure water, HNTs, HNT@Fe$_3$O$_4$, HNT@PPy, HNT@Fe$_3$O$_4$@PPy, and HNT@Fe$_3$O$_4$@PPy@DOX aqueous dispersion were evaluated, and the change in temperature under NIR light irradiation for 5 min was recorded using an infrared camera. As shown in Figure S4, the temperature of ultrapure water and HNTs slightly changes after laser irradiation, whereas HNT@Fe$_3$O$_4$, HNT@PPy, and HNT@Fe$_3$O$_4$@PPy have a much higher temperature than ultrapure water. Interestingly, HNT@Fe$_3$O$_4$@PPy and HNT@Fe$_3$O$_4$@PPy@DOX aqueous dispersion show the best photothermal performance, because both PPy and Fe$_3$O$_4$ exhibit strong photothermal conversion efficiency. Therefore, HNT@Fe$_3$O$_4$@PPy@DOX was employed to evaluate the in vitro cytotoxic sensitivity and in vivo antitumor effect in subsequent experiments. In addition, the temperature of laser-irradiated nanoparticle suspension increased as the concentration of HNT@Fe$_3$O$_4$@PPy@DOX and the laser power increased (Figure 4A,C). After 8 min of irradiation, the temperature of the HNT@Fe$_3$O$_4$@PPy@DOX is raised by ~21 °C (1.2 W/cm^2, 1 mg/mL). The HNT@Fe$_3$O$_4$@PPy@DOX aqueous dispersion has a stable change of temperature by five cycles of 808 nm laser irradiation (Figure 4D), which indicates that the photothermal effect of HNT@Fe$_3$O$_4$@PPy@DOX is steady and repeatable during PTT.

3.2. Biocompatibility and Characterization of HNT@Fe$_3$O$_4$@PPy@DOX Composites. To further investigate the cytotoxicity of HNTs and HNT@Fe$_3$O$_4$@PPy nanomaterials in vitro, MCF10A and MCF-7 cells were incubated with different concentrations of HNTs and HNT@Fe$_3$O$_4$@PPy for 24 h and determined by CCK-8 kit. As shown in Figure 5A, B,
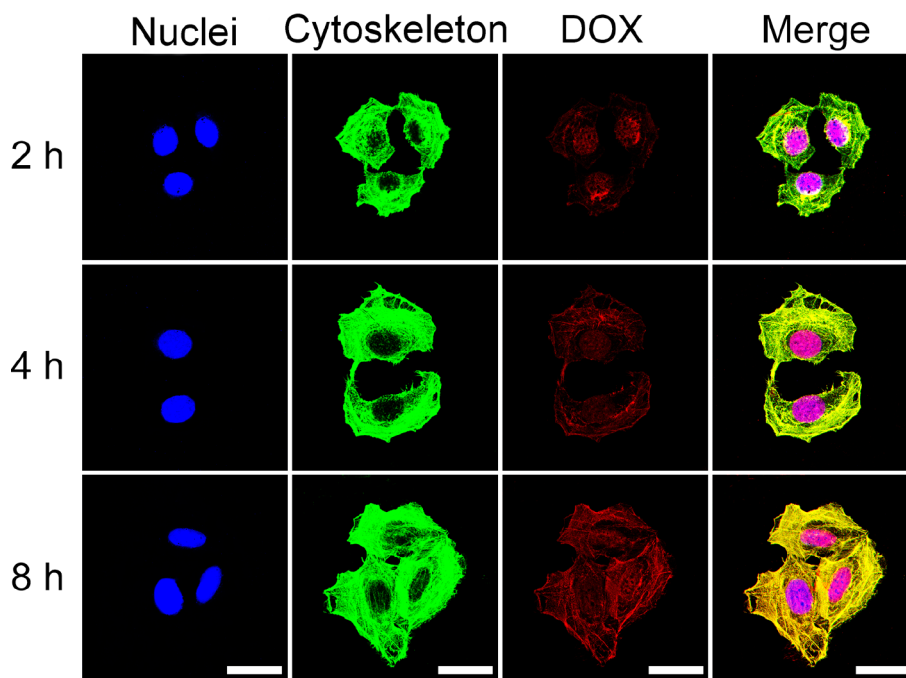
Figure 6. Fluorescence images of MCF-7 cells treated with HNT@Fe$_3$O$_4$@PPy@DOX at different time intervals. Scale bar: 20 μm.

HNTs and HNT@Fe$_3$O$_4$@PPy show low-level toxicity toward both the normal cells and tumor cells even at high concentrations. The results in Figure 5C show that the cell viability of HNTs (93.8%) under laser irradiation is still high, suggesting no photothermal effect of raw HNTs. The cell viability of the HNT@Fe$_3$O$_4$@PPy@DOX with a nonlaser irradiation group is 63.1% (Figure 5C) because of the antitumor effect of the DOX drug, whereas that of HNT@Fe$_3$O$_4$@PPy@DOX with the laser irradiation group is 10% because of the combination of photothermal and chemotherapy. It is intuitively observed by AO/EB live-staining that cells cocultured with PBS and HNTs mainly show green fluorescence after 8 min of laser irradiation. HNT@Fe$_3$O$_4$@PPy@DOX without a laser irradiation group shows only a small amount of red fluorescent cells, whereas HNT@Fe$_3$O$_4$@PPy@DOX treated with laser irradiation group displays almost dead cells, which is consistent with the data of CCK-8 assay (Figure 5D). Furthermore, the apoptosis rate of PBS and HNTs after laser irradiation is 3.79 and 10.04%, respectively, whereas HNT@Fe$_3$O$_4$@PPy@DOX without laser irradiation causes apoptotic cells in 34.07%. After laser irradiation, HNT@Fe$_3$O$_4$@PPy@DOX results in 75.1% apoptosis rate (Figure 5E). In addition, results from 4T1 cell (a mouse breast cancer cell) also display the similar tendency (Figure S5), which provides evidence for the subsequent experiments in mice. The cellular uptake was evaluated in MCF-7 cells incubated with HNT@Fe$_3$O$_4$@PPy@DOX for different times (2, 4, and 8 h). The temperature in cells treated with HNT@Fe$_3$O$_4$@PPy@DOX is raised by irradiation, which promotes the release of DOX from HNT@Fe$_3$O$_4$@PPy@DOX and then causes a large number of cancer cell deaths. Results shown in Figure 6 indicate that DOX released from HNT@Fe$_3$O$_4$@PPy@DOX is enriched in both cytoplasm and nucleus as the incubation time increases. DOX injures cancer cells via both the mitochondrial and nucleus mechanisms, which can improve the anticancer efficiency.[34,47] Therefore, it is concluded that HNT@Fe$_3$O$_4$@PPy@DOX treated with irradiation would have an excellent antitumor effect by the synergic effect of chemotherapy and PTT.

3.3. In Vivo Chemo-Photothermal Treatment. Chemotherapy is widely utilized to treat cancer in the clinic, but chemotherapy drugs lack selectivity for tumor cells and induce lots of side effects.[48] Delivery of drugs under magnetic targeting has become a hot topic in tumor-targeted therapy.[48−50] Nanoparticles anchored with magnetic targeting ligand molecules such as Fe$_3$O$_4$ can be delivered to tumor sites by a locally applied external magnetic field, thereby achieving tumor-targeted efficacy.[51−53] The cytotoxic sensitivity of MCF-7 cells and 4T1 cells to DOX has no significant difference.[34,49,54] Tumor-bearing mice (with normal immunity) can be easily established with 4T1 cells, whereas MCF-7-bearing mice need the higher-cost nude mice. Therefore, the tumor-bearing mice were established using 4T1 cells to investigate the tumor-targeted efficacy, toxicity, and antitumor effect in vivo.

First, in order to investigate the potential magnetic targeting efficiency of HNT@Fe$_3$O$_4$@PPy@DOX nanoplatform, we intravenously 4T1-bearing mice injected with HNT@Fe$_3$O$_4$@PPy@DOX (22.5 mg/kg). After that, a plate-shaped magnet was immobilized on the tumor area of each mouse, and the schematic diagram of a magnet-attached tumor-bearing mouse is shown in Figure S6. T_2-weighted MRI images were captured at indicated time points after the intravenous injection. As shown in Figure 7A, B, dramatically increased darkening effects in the transversal and longitudinal T_2-weighted MRI images were observed around the tumor sites after the intravenous injection of the HNT@Fe$_3$O$_4$@PPy@DOX. Additionally, the darkening effects in tumor area increases with time and reaches a maximum at 24 h after the administration of HNT@Fe$_3$O$_4$@PPy@DOX. These results suggest the high uptake of HNT@Fe$_3$O$_4$@PPy@DOX nanoparticles in the tumor by an external magnetic field. Furthermore, the MR signal of mice treated with HNT@Fe$_3$O$_4$@PPy@DOX in 24 h is 3.59 times higher in the transversal and 3.72 times higher in longitudinal of T_2-
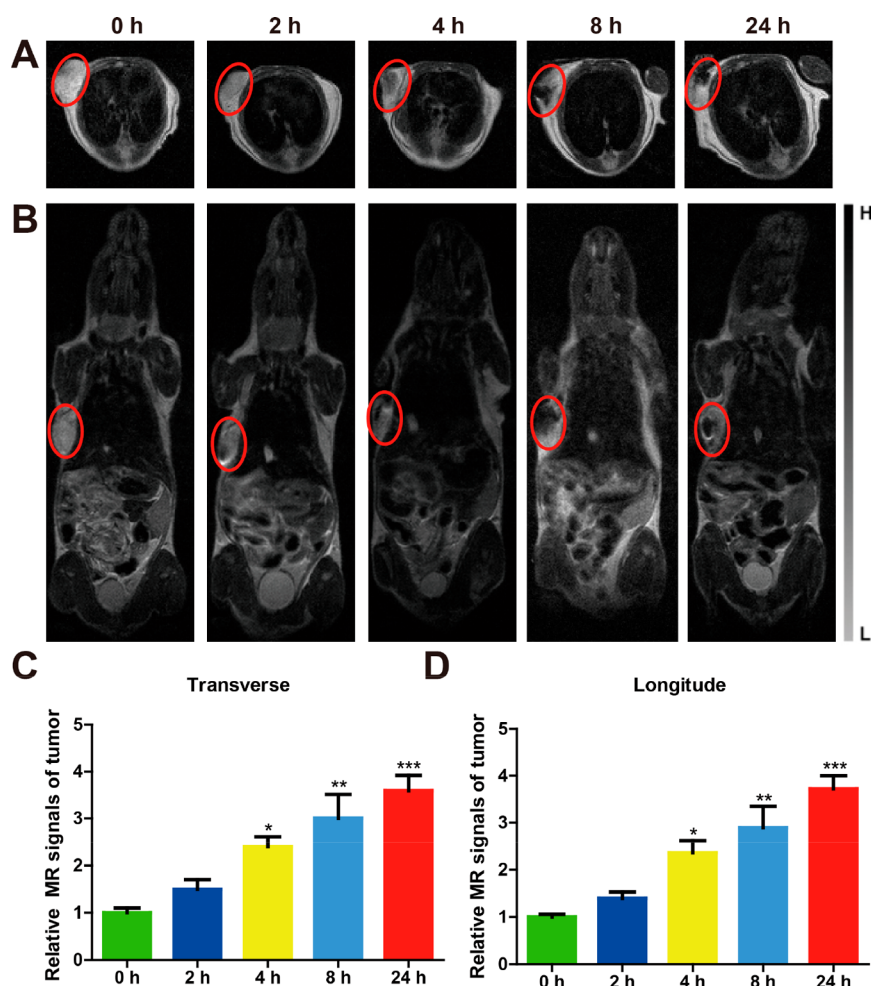
Figure 7. Magnetic tumor-targeted efficiency of HNT@Fe$_3$O$_4$@PPy@DOX in 4T1-bearing mice. (A) Transversal and (B) longitudinal T_2-weighted images were captured by M3 Compact MRI System at indicated time points (0, 2, 4, 8, and 24 h) after being intravenously injected with HNT@Fe$_3$O$_4$@PPy@DOX (22.5 mg/kg). Tumors in T_2-weighted images are highlighted by red circles. (C) Transversal and (D) longitudinal MR signals in the tumor area are quantified by *ImageJ* software at indicated time points after intravenously injected with HNT@Fe$_3$O$_4$@PPy@DOX (22.5 mg/kg). The data are represented as mean ± SD ($n = 3$) and analyzed by one-way ANOVA with Tukey's post hoc test. *$P < 0.05$, **$P < 0.01$, ***$P < 0.001$ vs 0 h.

weighted images ($P < 0.05$) than the mice at 0 h. These data strongly suggest that HNT@Fe$_3$O$_4$@PPy@DOX exhibits excellent magnetic tumor-targeted efficiency and could be considered as a promising application in magnetic targeting tumor therapy.

Enhancing the permeability and retention effects of nanoparticles can enhance the accumulation of drug in tumors and improved antitumor efficacy.[55,56] In order to investigate the biodistribution and tumor-targeted efficiency of HNT@Fe$_3$O$_4$@PPy@DOX in vivo, 4T1-bearing mice were intravenously injected with DOX (0.52 mg/kg) and HNT@Fe$_3$O$_4$@PPy@DOX (0.52 mg DOX equiv/kg). After that, a plate-shaped magnet was immobilized on the tumor area of each mouse by using adhesive tape. DOX fluorescence of main tissues (heart, liver, spleen, lung, kidney, and tumor) was detected by in vivo fluorescence imaging system at indicated time points, which was used to evaluate the time-dependent biodistribution and tumor-targeted efficiency of HNT@Fe$_3$O$_4$@PPy@DOX in the 4T1-bearing mice. As expected, the accumulation of DOX fluorescence in the tumor of HNT@Fe$_3$O$_4$@PPy@DOX treated mice is obviously higher than that treated with free DOX treatment (8, 12, and 24 h) ($P < 0.01$)

(Figure 8A,B). Additionally, DOX fluorescence in tumor area achieves the maximum at 8 h after the administration of HNT@Fe$_3$O$_4$@PPy@DOX, whereas the free DOX treatment reaches the maximum at 4 h. Moreover, HNT@Fe$_3$O$_4$@PPy@DOX treatment reveals a remarkably higher DOX fluorescence intensity in the tumor than that in other tissues (heart, liver, spleen, lung, and kidney) (Figure 8C). According to the above results, the change in DOX fluorescence in the major tissues reveals the biodistribution and elimination of HNT@Fe$_3$O$_4$@PPy@DOX at indicated time points (4, 8, 12, and 24 h). It is considered that HNT@Fe$_3$O$_4$@PPy@DOX in blood circulation systems could transfer from main tissues to tumor because of the external magnet in tumor sites. Therefore, these results reveal that HNT@Fe$_3$O$_4$@PPy@DOX has excellent tumor-targeted performance.

On the basis of the in vitro promising photothermal performance and in vivo tumor-targeted efficiency of HNT@Fe$_3$O$_4$@PPy@DOX, a further exploration of photothermal conversion efficiency was carried out in 4T1-bearing mice. Mice were injected with normal saline (300 μL) and HNT@Fe$_3$O$_4$@PPy@DOX (22.5 mg/kg) through intravenous injection. As shown in Figure 9A,B, the tumor temperature of
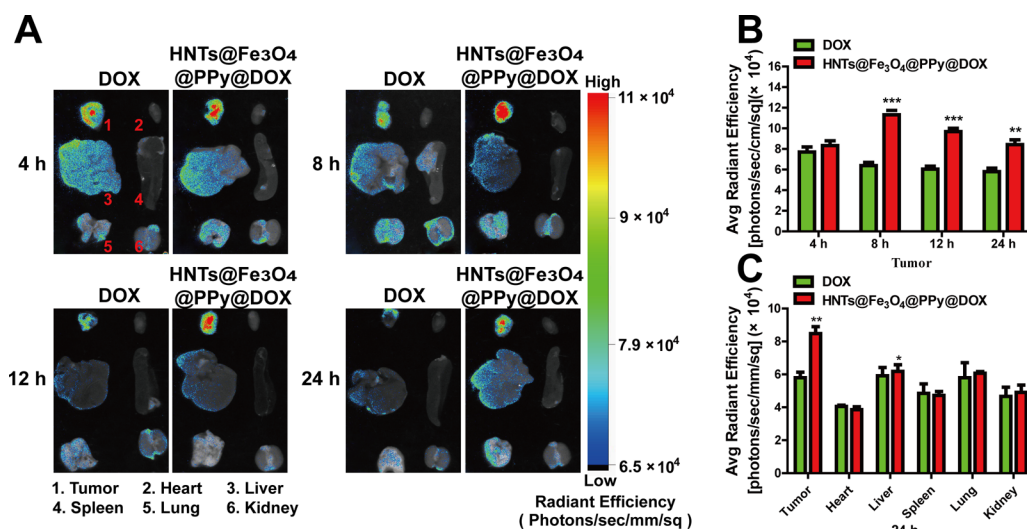
Figure 8. Biodistribution of HNT@Fe$_3$O$_4$@PPy@DOX in 4T1-bearing mice after intravenous injection. (A) Fluorescence imaging of major tissues and tumors of 4T1-bearing mice after intravenous injection of DOX (0.52 mg/kg) and HNT@Fe$_3$O$_4$@PPy@DOX (0.52 mg DOX equiv/kg) at indicated time points (4, 8, 12, and 24 h). (B) Quantification of DOX fluorescence of tumors at indicated time points (4, 8, 12, and 24 h). (C) Quantification of DOX fluorescence of major tissues and tumors at 24 h. The results are represented as mean ± SD (n = 3) and analyzed by t-test. *P < 0.05, **P < 0.01, ***P < 0.001 vs DOX.
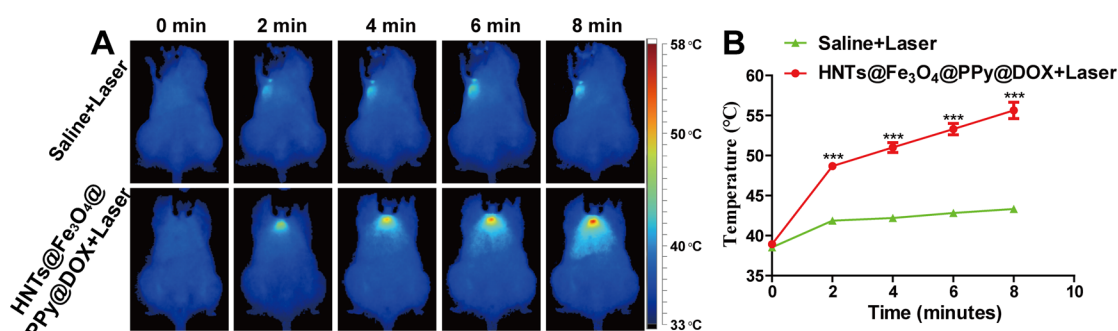
Figure 9. Photothermal performance of HNT@Fe$_3$O$_4$@PPy@DOX in 4T1-bearing mice. (A) Thermographs were captured by an NIR thermal camera at continuous time intervals (0, 2, 4, 6, and 8 min). (B) Temperature curves in tumor tissues of mice monitored during photothermal treatment. The data are shown as mean ± SD (n = 3) and analyzed using two-way ANOVA with Tukey's post hoc test. ***P < 0.001 vs saline + laser.

mice administrated with HNT@Fe$_3$O$_4$@PPy@DOX exhibits a rapid increase after irradiation for 8 min (P < 0.001). It is noted that the temperature at the local surface tumor of mice treated with HNT@Fe$_3$O$_4$@PPy@DOX is dramatically increased to 55.6 ± 0.8 °C within 8 min laser irradiation, which is sufficient to kill the tumor effectively because of the ischemic supplement of the tumor area.[57] Therefore, all these results definitely demonstrate that HNT@Fe$_3$O$_4$@PPy@DOX holds an excellent photothermal performance and it could be a promising antitumor nanoplatform.

Encouraged by the tumor-targeted efficiency of HNT@Fe$_3$O$_4$@PPy@DOX and its high photothermal conversion efficiency in vivo, the synergistic chemo-photothermal therapeutic effects of 4T1-bearing mice were further investigated. Upon the tumor sizes reaching ~100 mm^3, mice were administrated with normal saline (300 μL, laser irradiation, 1 W/cm^2, 8 min), HNT@Fe$_3$O$_4$@PPy (22.5 mg/kg), DOX (0.52 mg/kg), HNT@Fe$_3$O$_4$@PPy@DOX (0.52 mg DOX equiv/kg), and HNT@Fe$_3$O$_4$@PPy@DOX + laser (0.52 mg DOX equiv/kg, laser irradiation, 1 W/cm^2, 8 min) through intravenous injection every other day. As indicated in Figure 10A, the body weight of the DOX group obviously decreases

(P < 0.01) compared with the normal saline + laser group, whereas HNT@Fe$_3$O$_4$@PPy, HNT@Fe$_3$O$_4$@PPy@DOX, and HNT@Fe$_3$O$_4$@PPy@DOX + laser groups have no significant influence on the body weight. These results indicate that DOX can induce a significant decrease in body weight at an even low concentrations of 0.52 mg/kg, which agrees with previous studies about certain toxic effects on mice.[49] However, HNT@Fe$_3$O$_4$@PPy@DOX treatment shows no obvious toxicity to mice, which demonstrates that HNT@Fe$_3$O$_4$@PPy may be a superior drug carrier nanoplatform in antitumor therapy. As expected, HNT@Fe$_3$O$_4$@PPy@DOX treatment significantly reduces (P < 0.001) both tumor volume and tumor weight in 4T1-bearing mice by comparing to the normal saline + laser treatment, whereas DOX and HNT@Fe$_3$O$_4$@PPy treatments indicate no obvious change (Figure 10B,D). These results indicate that HNT@Fe$_3$O$_4$@PPy@DOX can be considered as a promising tumor-targeted nanomaterial in cancer treatment without producing toxicity. Furthermore, mice treated with HNT@Fe$_3$O$_4$@PPy@DOX + laser exhibits the best antitumor effects, which can be attributed to the synergistic chemo-photothermal therapeutic effects. Collectively, these data
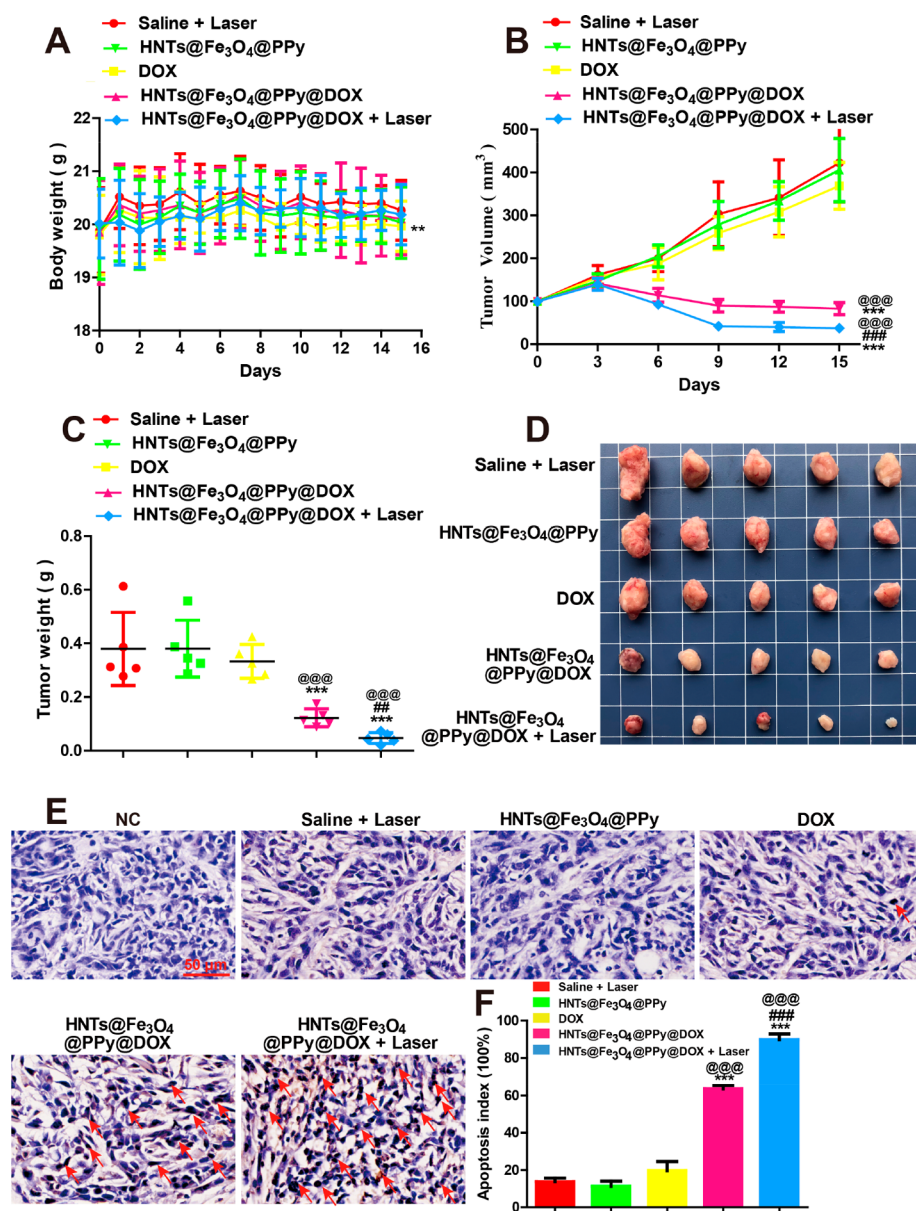
Figure 10. Synergistic chemo-photothermal therapeutic efficiency of HNT@Fe$_3$O$_4$@PPy@DOX in 4T1-bearing mice. (A) Body weight and (B) tumor volume curves of 4T1-bearing mice administrated with normal saline (300 μL and laser irradiation, 1 W/cm^2, 8 min), HNT@Fe$_3$O$_4$@PPy (22.5 mg/kg), DOX (0.52 mg/kg), HNT@Fe$_3$O$_4$@PPy@DOX (0.52 mg DOX equiv/kg), and HNT@Fe$_3$O$_4$@PPy@DOX + laser group (0.52 mg DOX equiv/kg, laser irradiation, 1 W/cm^2, 8 min) through intravenous injection every other day during treatment period. (C) Tumor weight and (D) photographs of 4T1-bearing mice on the 16th day. (E) Representative photographs of TUNEL assay of tumor sections. (F) Number of apoptosis cells in different treatments that were counted blindly in five randomly selected regions. Scale bar: 50 μm. The data are shown by mean $\pm$ SD ($n = 5$), the body weight and the tumor volume were performed using two-way ANOVA with Tukey's post hoc test, the tumor weight and apoptosis index were analyzed using one-way ANOVA with Tukey's post hoc test. **$P < 0.01$, ***$P < 0.001$ vs saline + Laser, ##$P < 0.01$, ###$P < 0.001$ vs HNT@Fe$_3$O$_4$@PPy@DOX, @@@$P < 0.001$ vs DOX.

indicate that HNT@Fe$_3$O$_4$@PPy@DOX appears to be greatly efficient in suppressing tumors.

Subsequently, the apoptosis index of HNT@Fe$_3$O$_4$@PPy@DOX in tumor tissues was performed by TdT-mediated dUTP nick-end labeling (TUNEL) assay to further confirm the antitumor efficacy. The apoptotic cells were indicated by brown spots (the red arrows) in tumor tissues. HNT@Fe$_3$O$_4$@PPy@DOX and HNT@Fe$_3$O$_4$@PPy@DOX + laser treatments induce significant apoptosis ($P < 0.001$) in tumor tissues in comparison to the normal saline + laser treatment (Figure 10E, F). HNT@Fe$_3$O$_4$@PPy@DOX + laser treatment exhibits more prominent apoptosis than HNT@Fe$_3$O$_4$@PPy@DOX treat-

ment ($P < 0.01$), which agrees with the change in tumor volume and tumor weight. These results reveal that HNT@Fe$_3$O$_4$@PPy@DOX showed an excellent antitumor efficacy by inducing apoptosis of cancer cells.

3.4. In Vivo Hemocompatibility and Toxicity Assay of HNT@Fe$_3$O$_4$@PPy@DOX.
The potential long-term toxicity and hemocompatibility of nanoparticles in vivo are significant for practical biomedical application.[58−60] To reveal the hemocompatibility of HNT@Fe$_3$O$_4$@PPy@DOX, we performed the blood smear, serum biochemistry, and complete blood panel assay by two groups of BALB/c mice ($n = 3$). Mice were treated with normal saline (300 μL) or HNT@

Fe_3O_4@PPy@DOX (22.5 mg/kg) via intravenous injection every other day for 15 days. The results of blood smears reveal that HNT@Fe_3O_4@PPy@DOX does not change the morphology of platelets, leukocytes, and white blood cells in comparison to control group (Figure S7A). In addition, no signs of coagulation are found in the blood smears of the HNT@Fe_3O_4@PPy@DOX group. A variety of biochemistry parameters are selected to reflect the liver and kidney function (Figure S7B, D), and there is no noticeable hepatic toxicity and nephrotoxicity induced by HNT@Fe_3O_4@PPy@DOX treatment. As for the hematological index (Figure S7E, L), all these parameters in HNT@Fe_3O_4@PPy@DOX-treated mice are in normal ranges. On the basis of the biochemistry and hematological assays, we conclude that HNT@Fe_3O_4@PPy@DOX is biosafe and biocompatible.

To further evaluate the potential toxicity and biosafety of the HNT@Fe_3O_4@PPy@DOX in vivo, we investigated the histological analysis of main tissues (tumor, heart, liver, spleen, lung, and kidney) by H&E staining. As shown in Figure S8, it is noted that the HNT@Fe_3O_4@PPy@DOX and HNT@Fe_3O_4@PPy@DOX + laser treatments induce obvious necrosis in tumor tissues, whereas the normal saline + laser, HNT@Fe_3O_4@PPy, and DOX treatments present no obvious changes. As for the normal tissues, DOX treatment can induce obvious heart damage (rupture and dispersion of the cardiomyocytes) and visible nephrotoxicity (distinct necrosis of certain glomerulus), whereas the normal saline + laser, HNT@Fe_3O_4@PPy, HNT@Fe_3O_4@PPy@DOX, and HNT@Fe_3O_4@PPy@DOX + laser treatments exhibit no significant toxicity. Few studies in the literature have reported on how halloysite is decomposed or removed from the human body after intravenous injection. However, no obvious toxicity of halloysite was found toward the lung and liver of mice at low dose (5 mg/kg BW) by oral administration.[61,62] In total, HNT@Fe_3O_4@PPy@DOX provides a multifunctional nanoplatform that can achieve a biosafe, magnetic tumor-targeted, excellent photothermal performance in breast cancer therapy.

In our previous work, we reported that a chemotherapy nanoplatform based on modified halloysite by poly(ethylene glycol) (PEG) and folate (FA) conjugation (DOX@HNTs-PEG-FA) for treatment of the breast cancer, in which PEG and FA were used for long-circulating and tumor-targeting purposes, respectively.[63] However, it is considered that a single model of chemotherapy has some drawbacks such as drug resistance, low efficacy, and side effects to normal tissues. Among various treatment strategies, the combined therapy has been recognized as a promising strategy to amplify the anticancer efficiency and minimize systemic side effects of chemotherapeutic agents by reducing the drug dosage. Therefore, the multifunctional nanoplatform of HNT@Fe_3O_4@PPy@DOX was explored in this work, which combined photothermal therapy with chemotherapy as well as magnetic targeting and MRI imaging.

In total, the HNT@Fe_3O_4@PPy@DOX exhibits enhanced antitumor effects and lowered toxicity as evidenced by highly efficient tumor ablation ability along with good biocompatibility and no obvious histological damage to the major organs because of the magnetic targeting effects. In vivo therapeutic experiments demonstrate that HNT@Fe_3O_4@PPy@DOX can achieve prominent antitumor effects even at a relatively low DOX concentration of 0.52 mg/kg and reduce the toxicity to normal tissues. In contrast, the drug concentration for treatment of the same tumor was 5 mg/kg in DOX@HNTs-

PEG-FA. Moreover, the average tumor volume of HNT@Fe_3O_4@PPy@DOX treatment on 15th day decreased to 37.23 from 101.31 mm^3 (Figure 10B), whereas the tumor volume of the DOX@HNTs-PEG-FA-treated group increased from 50.41 to 139.64 mm^3 at the same administrated interval. Besides, Fe_3O_4 is nondegradable material, so it can accumulate in tumor tissue because of the external magnet and exerts a continuously targeted photothermal ablation to cancer cells for long time. HNT@Fe_3O_4@PPy@DOX does not show significant toxicity in serum biochemistry and complete blood panel assay in normal mice, although it exhibits a T_2-weighted MRI imaging-guided function that could achieve magnetic targeting photothermal therapy of cancer spatially and timely controlled by the external magnetic field.

4. CONCLUSIONS

A multifunctional nanoplatform for targeting delivery and high-efficiency chemo-photothermal therapy toward breast cancer is designed by in situ formation of Fe_3O_4 nanoparticles on the surfaces of HNTs, followed by loading DOX and wrapping a layer of PPy outside the tubes. The structure and properties of HNT@Fe_3O_4@PPy@DOX are characterized by different techniques. In vitro experiments demonstrate that HNT@Fe_3O_4@PPy@DOX nanocomposites exhibited strong cancer cell-killing effects under NIR laser irradiation. Laser irradiation promotes the release of DOX from HNT@Fe_3O_4@PPy@DOX nanocomposites, allowing combined chemo-photothermal therapy in tumor treatments. HNT@Fe_3O_4@PPy@DOX has good biocompatibility and does not show significant toxicity in serum biochemistry and the complete blood panel assay in normal mice. In vivo therapeutic experiments demonstrate that HNT@Fe_3O_4@PPy@DOX can achieve prominent antitumor effects even at relatively low DOX concentration and reduce the toxicity to normal tissues. In conclusion, the construction of HNT@Fe_3O_4@PPy@DOX therapeutic nanoplatform provided a rapid, effective, biocompatible, and cheap choice for clinical targeting therapy toward breast cancer.

■ ASSOCIATED CONTENT

ⓢ Supporting Information

The Supporting Information is available free of charge at https://pubs.acs.org/doi/10.1021/acsbiomaterials.9b01709.

> Digital photograph of HNT@Fe_3O_4@PPy@DOX with or without magnets dispersed in PBS; digital photographs of HNT@Fe_3O_4@PPy@DOX dispersed in PBS at different temperatures; TEM images of HNT@Fe_3O_4 and HNT@Fe_3O_4@PPy nanospheres; zeta potential and particle size for HNTs, HNT@PPy, and HNT@Fe_3O_4@PPy@DOX; temperature increase of H_2O, HNTs, HNT@Fe_3O_4, HNT@PPy, HNT@Fe_3O_4@PPy, and HNT@Fe_3O_4@PPy@DOX in the aqueous dispersion; relative survival of 4T1 cells in different treatment; schematic diagram of a magnet-attached tumor-bearing mouse; in vivo hemocompatibility and toxicity assay of HNT@Fe_3O_4@PPy@DOX; histopathological analysis of HNT@Fe_3O_4@PPy@DOX in 4T1-bearing mice (PDF)

■ AUTHOR INFORMATION

Corresponding Authors

Mingxian Liu − *Department of Materials Science and Engineering, Jinan University, Guangzhou 510632, China;* orcid.org/0000-0002-5466-3024; Email: liumx@jnu.edu.cn

Rong-Rong He − *Guangdong Engineering Research Center of Chinese Medicine & Disease Susceptibility, Guangdong Province Key Laboratory of Pharmacodynamic Constituents of TCM and New Drugs Research, College of Pharmacy, and International Cooperative Laboratory of Traditional Chinese Medicine Modernization and Innovative Drug Development of Chinese Ministry of Education (MOE), College of Pharmacy, Jinan University, Guangzhou 510632, China;* Email: rongronghe@jnu.edu.cn

Authors

Xiang Luo − *Guangdong Engineering Research Center of Chinese Medicine & Disease Susceptibility, Guangdong Province Key Laboratory of Pharmacodynamic Constituents of TCM and New Drugs Research, College of Pharmacy, and International Cooperative Laboratory of Traditional Chinese Medicine Modernization and Innovative Drug Development of Chinese Ministry of Education (MOE), College of Pharmacy, Jinan University, Guangzhou 510632, China*

Jun Zhang − *Department of Materials Science and Engineering, Jinan University, Guangzhou 510632, China*

Yan-Ping Wu − *Guangdong Engineering Research Center of Chinese Medicine & Disease Susceptibility, Guangdong Province Key Laboratory of Pharmacodynamic Constituents of TCM and New Drugs Research, College of Pharmacy, and International Cooperative Laboratory of Traditional Chinese Medicine Modernization and Innovative Drug Development of Chinese Ministry of Education (MOE), College of Pharmacy, Jinan University, Guangzhou 510632, China*

Xiaohan Yang − *Department of Materials Science and Engineering, Jinan University, Guangzhou 510632, China*

Xiu-Ping Kuang − *Guangdong Engineering Research Center of Chinese Medicine & Disease Susceptibility, Jinan University, Guangzhou 510632, China; Yunnan University of Traditional Chinese Medicine, Kunming 650550, China*

Wei-Xi Li − *Yunnan University of Traditional Chinese Medicine, Kunming 650550, China*

Yi-Fang Li − *Guangdong Engineering Research Center of Chinese Medicine & Disease Susceptibility, Guangdong Province Key Laboratory of Pharmacodynamic Constituents of TCM and New Drugs Research, College of Pharmacy, and International Cooperative Laboratory of Traditional Chinese Medicine Modernization and Innovative Drug Development of Chinese Ministry of Education (MOE), College of Pharmacy, Jinan University, Guangzhou 510632, China*

Complete contact information is available at:
https://pubs.acs.org/10.1021/acsbiomaterials.9b01709

Author Contributions

Conception and design by X.L., J.Z., Y.P.W, W.X.L, Y.F.L, R.R.H., and M.X.L.; experiments by X.L., J.Z., X.H.Y., and X.P.K.; analysis by X.L. and J.Z.; writing by X.L. and J.Z., with contributions from X.L., J.Z., R.R.H., and M.X.L; review and editing by X.L., J.Z., Y.P.W., R.R.H., and M.X.L.; supervision by R.R.H. and M.X.L; funding acquisition by R.R.H. and M.X.L.

Author Contributions

†X.L., J.Z., and Y.P.W. contributed equally to this work.

Notes

The authors declare no competing financial interest.

■ REFERENCES

(1) Aioub, M.; Panikkanvalappil, S. R.; El-Sayed, M. A. Platinum-coated gold nanorods: efficient reactive oxygen scavengers that prevent oxidative damage toward healthy, untreated cells during plasmonic photothermal therapy. *ACS Nano* **2017**, *11* (1), 579−586.

(2) Nam, J.; Won, N.; Jin, H.; Chung, H.; Kim, S. pH-induced aggregation of gold nanoparticles for photothermal cancer therapy. *J. Am. Chem. Soc.* **2009**, *131* (38), 13639−13645.

(3) Chatterjee, D. K.; Diagaradjane, P.; Krishnan, S. Nanoparticle-mediated hyperthermia in cancer therapy. *Ther. Delivery* **2011**, *2* (8), 1001−1014.

(4) Wang, D.; Dong, H.; Li, M.; Cao, Y.; Yang, F.; Zhang, K.; Dai, W.; Wang, C.; Zhang, X. Erythrocyte−Cancer Hybrid Membrane Camouflaged Hollow Copper Sulfide Nanoparticles for Prolonged Circulation Life and Homotypic-Targeting Photothermal/Chemo-therapy of Melanoma. *ACS Nano* **2018**, *12* (6), 5241−5252.

(5) Lin, H.; Gao, S.; Dai, C.; Chen, Y.; Shi, J. A two-dimensional biodegradable niobium carbide (MXene) for photothermal tumor eradication in NIR-I and NIR-II biowindows. *J. Am. Chem. Soc.* **2017**, *139* (45), 16235−16247.

(6) Chen, W.-H.; Luo, G.-F.; Lei, Q.; Hong, S.; Qiu, W.-X.; Liu, L.-H.; Cheng, S.-X.; Zhang, X.-Z. Overcoming the heat endurance of tumor cells by interfering with the anaerobic glycolysis metabolism for improved photothermal therapy. *ACS Nano* **2017**, *11* (2), 1419−1431.

(7) Zhang, A.; Li, A.; Zhao, W.; Liu, J. Recent advances in functional polymer decorated two-dimensional transition-metal dichalcogenides nanomaterials for chemo-photothermal therapy. *Chem. - Eur. J.* **2018**, *24* (17), 4215−4227.

(8) Li, P.; Liu, L.; Lu, Q.; Yang, S.; Yang, L.; Cheng, Y.; Wang, Y.; Wang, S.; Song, Y.; Tan, F.; Li, N. Ultrasmall MoS$_2$ Nanodots-Doped Biodegradable SiO$_2$ Nanoparticles for Clearable FL/CT/MSOT Imaging-Guided PTT/PDT Combination Tumor Therapy. *ACS Appl. Mater. Interfaces* **2019**, *11* (6), 5771−5781.

(9) Liu, X.; Su, H.; Shi, W.; Liu, Y.; Sun, Y.; Ge, D. Functionalized poly (pyrrole-3-carboxylic acid) nanoneedles for dual-imaging guided PDT/PTT combination therapy. *Biomaterials* **2018**, *167*, 177−190.

(10) Wang, Y.; Wei, G.; Zhang, X.; Huang, X.; Zhao, J.; Guo, X.; Zhou, S. Multistage targeting strategy using magnetic composite nanoparticles for synergism of photothermal therapy and chemo-therapy. *Small* **2018**, *14* (12), 1702994.

(11) Gulzar, A.; Xu, J.; Xu, L.; Yang, P.; He, F.; Yang, D.; An, G.; Ansari, M. B. Redox-responsive UCNPs-DPA conjugated NGO-PEG-BPEI-DOX for imaging-guided PTT and chemotherapy for cancer treatment. *Dalton Transactions* **2018**, *47* (11), 3921−3930.

(12) Fan, B.; Yang, X.; Li, X.; Lv, S.; Zhang, H.; Sun, J.; Li, L.; Wang, L.; Qu, B.; Peng, X.; Zhang, R. Photoacoustic-imaging-guided therapy of functionalized melanin nanoparticles: combination of photothermal ablation and gene therapy against laryngeal squamous cell carcinoma. *Nanoscale* **2019**, *11* (13), 6285−6296.

(13) Chu, C.; Ren, E.; Zhang, Y.; Yu, J.; Lin, H.; Pang, X.; Zhang, Y.; Liu, H.; Qin, Z.; Cheng, Y.; et al. Zinc (II)-Dipicolylamine Coordination Nanotheranostics: Toward Synergistic Nanomedicine by Combined Photo/Gene Therapy. *Angew. Chem.* **2019**, *131* (1), 275−278.

(14) Peng, J.; Xiao, Y.; Li, W.; Yang, Q.; Tan, L.; Jia, Y.; Qu, Y.; Qian, Z. Photosensitizer micelles together with ido inhibitor enhance cancer photothermal therapy and immunotherapy. *Adv. Sci.* **2018**, *5* (5), 1700891.

(15) Zong, L.; Wu, H.; Lin, H.; Chen, Y. A polyoxometalate-functionalized two-dimensional titanium carbide composite MXene for effective cancer theranostics. *Nano Res.* **2018**, *11* (8), 4149−4168.

(16) Liao, Y.-T.; Liu, C.-H.; Chin, Y.; Chen, S.-Y.; Liu, S. H.; Hsu, Y.-C.; Wu, K. C. Biocompatible and Multifunctional Gold Nanorods for Effective Photothermal Therapy of Oral Squamous Cell Carcinoma. *J. Mater. Chem. B* **2019**, *7* (28), 4451−4460.

(17) Hajfathalian, M.; Amirshaghaghi, A.; Naha, P. C.; Chhour, P.; Hsu, J. C.; Douglas, K.; Dong, Y.; Sehgal, C. M.; Tsourkas, A.; Neretina, S.; Cormode, D. P. Wulff in a cage gold nanoparticles as contrast agents for computed tomography and photoacoustic imaging. *Nanoscale* **2018**, *10* (39), 18749−18757.

(18) Li, H.; Wang, P.; Deng, Y.; Zeng, M.; Tang, Y.; Zhu, W.-H.; Cheng, Y. Combination of active targeting, enzyme-triggered release and fluorescent dye into gold nanoclusters for endomicroscopy-guided photothermal/photodynamic therapy to pancreatic ductal adenocarcinoma. *Biomaterials* **2017**, *139*, 30−38.

(19) Lan, M.; Zhao, S.; Zhang, Z.; Yan, L.; Guo, L.; Niu, G.; Zhang, J.; Zhao, J.; Zhang, H.; Wang, P.; et al. Two-photon-excited near-infrared emissive carbon dots as multifunctional agents for fluorescence imaging and photothermal therapy. *Nano Res.* **2017**, *10* (9), 3113−3123.

(20) Yang, J.; Su, H.; Sun, W.; Cai, J.; Liu, S.; Chai, Y.; Zhang, C. Dual chemodrug-loaded single-walled carbon nanohorns for multimodal imaging-guided chemo-photothermal therapy of tumors and lung metastases. *Theranostics* **2018**, *8* (7), 1966.

(21) Shen, S.; Kong, F.; Guo, X.; Wu, L.; Shen, H.; Xie, M.; Wang, X.; Jin, Y.; Ge, Y. CMCTS stabilized Fe₃O₄ particles with extremely low toxicity as highly efficient near-infrared photothermal agents for in vivo tumor ablation. *Nanoscale* **2013**, *5* (17), 8056−8066.

(22) Wu, L.; Zong, L.; Ni, H.; Liu, X.; Wen, W.; Feng, L.; Cao, J.; Qi, X.; Ge, Y.; Shen, S. Magnetic thermosensitive micelles with upper critical solution temperature for NIR triggered drug release. *Biomater. Sci.* **2019**, *7* (5), 2134−2143.

(23) Shen, S.; Huang, D.; Cao, J.; Chen, Y.; Zhang, X.; Guo, S.; Ma, W.; Qi, X.; Ge, Y.; Wu, L. Magnetic liposomes for light-sensitive drug delivery and combined photothermal−chemotherapy of tumors. *J. Mater. Chem. B* **2019**, *7* (7), 1096−1106.

(24) Gao, Q.; Zhang, X.; Yin, W.; Ma, D.; Xie, C.; Zheng, L.; Dong, X.; Mei, L.; Yu, J.; Wang, C.; et al. Functionalized MoS₂ nanovehicle with near-infrared laser-mediated nitric oxide release and photothermal activities for advanced bacteria-infected wound therapy. *Small* **2018**, *14* (45), 1802290.

(25) Shi, H.; Yan, R.; Wu, L.; Sun, Y.; Liu, S.; Zhou, Z.; He, J.; Ye, D. Tumor-targeting CuS nanoparticles for multimodal imaging and guided photothermal therapy of lymph node metastasis. *Acta Biomater.* **2018**, *72*, 256−265.

(26) Yang, S.; Li, Z.; Wang, Y.; Fan, X.; Miao, Z.; Hu, Y.; Li, Z.; Sun, Y.; Besenbacher, F.; Yu, M. Multifunctional Bi@PPy-PEG Core−Shell Nanohybrids for Dual-Modal Imaging and Photothermal Therapy. *ACS Appl. Mater. Interfaces* **2018**, *10* (2), 1605−1615.

(27) Yu, S.; Li, G.; Liu, R.; Ma, D.; Xue, W. Dendritic Fe₃O₄@ Poly(dopamine)@ PAMAM Nanocomposite as Controllable NO-Releasing Material: A Synergistic Photothermal and NO Antibacterial Study. *Adv. Funct. Mater.* **2018**, *28* (20), 1707440.

(28) Li, L.; Yang, Q.; Shi, L.; Zheng, N.; Li, Z.; Li, K.; Qiao, S.; Jia, T.; Sun, T.; Wang, Y. Novel phthalocyanine-based polymeric micelles with high near-infrared photothermal conversion efficiency under 808 nm laser irradiation for in vivo cancer therapy. *J. Mater. Chem. B* **2019**, *7* (14), 2247−2251.

(29) Jang, J.; Yoon, H. Multigram-Scale Fabrication of Monodisperse Conducting Polymer and Magnetic Carbon Nanoparticles. *Small* **2005**, *1* (12), 1195−1199.

(30) Du, Q.; Ma, T.; Fu, C.; Liu, T.; Huang, Z.; Ren, J.; Shao, H.; Xu, K.; Tang, F.; Meng, X. Encapsulating ionic liquid and Fe₃O₄ nanoparticles in gelatin microcapsules as microwave susceptible agent for MR imaging-guided tumor thermotherapy. *ACS Appl. Mater. Interfaces* **2015**, *7* (24), 13612−13619.

(31) Lun, H.; Ouyang, J.; Yang, H. Natural halloysite nanotubes modified as an aspirin carrier. *RSC Adv.* **2014**, *4* (83), 44197−44202.

(32) Liu, M.; Chang, Y.; Yang, J.; You, Y.; He, R.; Chen, T.; Zhou, C. Functionalized halloysite nanotube by chitosan grafting for drug delivery of curcumin to achieve enhanced anticancer efficacy. *J. Mater. Chem. B* **2016**, *4* (13), 2253−2263.

(33) Li, L.-Y.; Zhou, Y.-M.; Gao, R.-Y.; Liu, X.-C.; Du, H.-H.; Zhang, J.-L.; Ai, X.-C.; Zhang, J.-P.; Fu, L.-M.; Skibsted, L. H. Naturally occurring nanotube with surface modification as biocompatible, target-specific nanocarrier for cancer phototherapy. *Biomaterials* **2019**, *190*, 86−96.

(34) Yang, J.; Wu, Y.; Shen, Y.; Zhou, C.; Li, Y.-F.; He, R.-R.; Liu, M. Enhanced therapeutic efficacy of doxorubicin for breast cancer using chitosan oligosaccharide-modified halloysite nanotubes. *ACS Appl. Mater. Interfaces* **2016**, *8* (40), 26578−26590.

(35) Long, Z.; Wu, Y.-P.; Gao, H.-Y.; Li, Y.-F.; He, R.-R.; Liu, M. Functionalization of halloysite nanotubes via grafting of dendrimer for efficient intracellular delivery of siRNA. *Bioconjugate Chem.* **2018**, *29* (8), 2606−2618.

(36) Gratton, S. E.; Ropp, P. A.; Pohlhaus, P. D.; Luft, J. C.; Madden, V. J.; Napier, M. E.; DeSimone, J. M. The effect of particle design on cellular internalization pathways. *Proc. Natl. Acad. Sci. U. S. A.* **2008**, *105* (33), 11613−11618.

(37) Guo, M.; Wang, A.; Muhammad, F.; Qi, W.; Ren, H.; Guo, Y.; Zhu, G. Halloysite nanotubes, a multifunctional nanovehicle for anticancer drug delivery. *Chin. J. Chem.* **2012**, *30* (9), 2115−2120.

(38) Tian, X.; Wang, W.; Tian, N.; Zhou, C.; Yang, C.; Komarneni, S. Cr (VI) reduction and immobilization by novel carbonaceous modified magnetic Fe₃O₄/halloysite nanohybrid. *J. Hazard. Mater.* **2016**, *309*, 151−156.

(39) Xie, Y.; Qian, D.; Wu, D.; Ma, X. Magnetic halloysite nanotubes/iron oxide composites for the adsorption of dyes. *Chem. Eng. J.* **2011**, *168* (2), 959−963.

(40) Hayashi, K.; Nakamura, M.; Miki, H.; Ozaki, S.; Abe, M.; Matsumoto, T.; Sakamoto, W.; Yogo, T.; Ishimura, K. Magnetically responsive smart nanoparticles for cancer treatment with a combination of magnetic hyperthermia and remote-control drug release. *Theranostics* **2014**, *4* (8), 834.

(41) Liu, Y.; Liu, M. Conductive carboxylated styrene butadiene rubber composites by incorporation of polypyrrole-wrapped halloysite nanotubes. *Compos. Sci. Technol.* **2017**, *143*, 56−66.

(42) Wu, B.; Wan, B.; Lu, S.-T.; Deng, K.; Li, X.-Q.; Wu, B.-L.; Li, Y.-S.; Liao, R.-F.; Huang, S.-W.; Xu, H.-B. Near-infrared light-triggered theranostics for tumor-specific enhanced multimodal imaging and photothermal therapy. *Int. J. Nanomed.* **2017**, *12*, 4467.

(43) Wang, S.; Shang, L.; Li, L.; Yu, Y.; Chi, C.; Wang, K.; Zhang, J.; Shi, R.; Shen, H.; Waterhouse, G. I.; et al. Metal−Organic-Framework-Derived Mesoporous Carbon Nanospheres Containing Porphyrin-Like Metal Centers for Conformal Phototherapy. *Adv. Mater.* **2016**, *28* (38), 8379−8387.

(44) Wu, J.; Li, Q.; Fan, L.; Lan, Z.; Li, P.; Lin, J.; Hao, S. High-performance polypyrrole nanoparticles counter electrode for dye-sensitized solar cells. *J. Power Sources* **2008**, *181* (1), 172−176.

(45) Chen, C.; Tang, W.; Jiang, D.; Yang, G.; Wang, X.; Zhou, L.; Zhang, W.; Wang, P. Hyaluronic acid conjugated polydopamine functionalized mesoporous silica nanoparticles for synergistic targeted chemo-photothermal therapy. *Nanoscale* **2019**, *11* (22), 11012−11024.

(46) Lee, H. J.; Liu, Y.; Zhao, J.; Zhou, M.; Bouchard, R. R.; Mitcham, T.; Wallace, M.; Stafford, R. J.; Li, C.; Gupta, S.; Melancon, M. P. In vitro and in vivo mapping of drug release after laser ablation

thermal therapy with doxorubicin-loaded hollow gold nanoshells using fluorescence and photoacoustic imaging. *J. Controlled Release* **2013**, *172* (1), 152−158.

(47) Xiong, H.; Du, S.; Ni, J.; Zhou, J.; Yao, J. Mitochondria and nuclei dual-targeted heterogeneous hydroxyapatite nanoparticles for enhancing therapeutic efficacy of doxorubicin. *Biomaterials* **2016**, *94*, 70−83.

(48) You, Y.; He, L.; Ma, B.; Chen, T. High-Drug-Loading Mesoporous Silica Nanorods with Reduced Toxicity for Precise Cancer Therapy against Nasopharyngeal Carcinoma. *Adv. Funct. Mater.* **2017**, *27* (42), 1703313.

(49) Zhang, J.; Luo, X.; Wu, Y.-P.; Wu, F.; Li, Y.-F.; He, R.-R.; Liu, M. Rod in Tube: A Novel Nanoplatform for Highly Effective Chemo-Photothermal Combination Therapy toward Breast Cancer. *ACS Appl. Mater. Interfaces* **2019**, *11* (4), 3690−3703.

(50) Veiseh, O.; Gunn, J. W.; Zhang, M. Design and fabrication of magnetic nanoparticles for targeted drug delivery and imaging. *Adv. Drug Delivery Rev.* **2010**, *62* (3), 284−304.

(51) Fu, G.; Liu, W.; Li, Y.; Jin, Y.; Jiang, L.; Liang, X.; Feng, S.; Dai, Z. Magnetic Prussian blue nanoparticles for targeted photothermal therapy under magnetic resonance imaging guidance. *Bioconjugate Chem.* **2014**, *25* (9), 1655−1663.

(52) Yu, J.; Yin, W.; Zheng, X.; Tian, G.; Zhang, X.; Bao, T.; Dong, X.; Wang, Z.; Gu, Z.; Ma, X.; Zhao, Y. Smart MoS_2/Fe_3O_4 nanotheranostic for magnetically targeted photothermal therapy guided by magnetic resonance/photoacoustic imaging. *Theranostics* **2015**, *5* (9), 931.

(53) Li, W.-P.; Liao, P.-Y.; Su, C.-H.; Yeh, C.-S. Formation of oligonucleotide-gated silica shell-coated Fe_3O_4-Au core−shell nano-trisoctahedra for magnetically targeted and near-infrared light-responsive theranostic platform. *J. Am. Chem. Soc.* **2014**, *136* (28), 10062−10075.

(54) Du, G.; Lin, H.; Wang, M.; Zhang, S.; Wu, X.; Lu, L.; Ji, L.; Yu, L. Quercetin greatly improved therapeutic index of doxorubicin against 4T1 breast cancer by its opposing effects on HIF-1α in tumor and normal cells. *Cancer Chemother. Pharmacol.* **2010**, *65* (2), 277.

(55) Mei, K.-C.; Bai, J.; Lorrio, S.; Wang, J. T.-W.; Al-Jamal, K. T. Investigating the effect of tumor vascularization on magnetic targeting in vivo using retrospective design of experiment. *Biomaterials* **2016**, *106*, 276−285.

(56) Sun, T.; Zhang, Y. S.; Pang, B.; Hyun, D. C.; Yang, M.; Xia, Y. Engineered nanoparticles for drug delivery in cancer therapy. *Angew. Chem., Int. Ed.* **2014**, *53* (46), 12320−12364.

(57) Lokerse, W. J.; Kneepkens, E. C.; ten Hagen, T. L.; Eggermont, A. M.; Grüll, H.; Koning, G. A. In depth study on thermosensitive liposomes: optimizing formulations for tumor specific therapy and in vitro to in vivo relations. *Biomaterials* **2016**, *82*, 138−150.

(58) Kumar, R.; Roy, I.; Ohulchanskky, T. Y.; Vathy, L. A.; Bergey, E. J.; Sajjad, M.; Prasad, P. N. In vivo biodistribution and clearance studies using multimodal organically modified silica nanoparticles. *ACS Nano* **2010**, *4* (2), 699−708.

(59) Liu, Z.; Dong, K.; Liu, J.; Han, X.; Ren, J.; Qu, X. Anti-Biofouling Polymer-Decorated Lutetium-Based Nanoparticulate Contrast Agents for In Vivo High-Resolution Trimodal Imaging. *Small* **2014**, *10* (12), 2429−2438.

(60) Zhang, H.; Ji, Z.; Xia, T.; Meng, H.; Low-Kam, C.; Liu, R.; Pokhrel, S.; Lin, S.; Wang, X.; Liao, Y.-P.; et al. Use of metal oxide nanoparticle band gap to develop a predictive paradigm for oxidative stress and acute pulmonary inflammation. *ACS Nano* **2012**, *6* (5), 4349−4368.

(61) Wang, X.; Gong, J.; Rong, R.; Gui, Z.; Hu, T.; Xu, X. Halloysite nanotubes-induced Al accumulation and fibrotic response in lung of mice after 30-day repeated oral administration. *J. Agric. Food Chem.* **2018**, *66* (11), 2925−2933.

(62) Wang, X.; Gong, J.; Gui, Z.; Hu, T.; Xu, X. Halloysite nanotubes-induced Al accumulation and oxidative damage in liver of mice after 30-day repeated oral administration. *Environ. Toxicol.* **2018**, *33* (6), 623−630.

(63) Wu, Y.-P.; Yang, J.; Gao, H.-Y.; Shen, Y.; Jiang, L.; Zhou, C.; Li, Y.-F.; He, R.-R.; Liu, M. Folate-Conjugated Halloysite Nanotubes, an Efficient Drug Carrier, Deliver Doxorubicin for Targeted Therapy of Breast Cancer. *ACS Applied Nano Materials* **2018**, *1* (2), 595−608.

Supporting information

Multifunctional HNTs@Fe$_3$O$_4$@PPy@DOX nanoplatform for Effective Chemo-Photothermal Combination Therapy of Breast Cancer with MR imaging

Xiang Luo,[†,∥,∥∥,§] Jun Zhang,[‡,§] Yan-Ping Wu,[†,∥,∥∥,§] Xiaohan Yang,[‡] Xiu-Ping Kuang,[†,⊥] Wei-Xi Li,[⊥] Yi-Fang Li,[†,∥,∥∥] Rong-Rong He,*[,†,∥,∥∥] Mingxian Liu*[,‡]

[†]Guangdong Engineering Research Center of Chinese Medicine & Disease Susceptibility, Jinan University, Guangzhou 510632, China

[‡]Department of Materials Science and Engineering, Jinan University, Guangzhou 510632, China

[∥]Guangdong Province Key Laboratory of Pharmacodynamic Constituents of TCM and New Drugs Research, College of Pharmacy, Jinan University, Guangzhou 510632, China

[∥∥]International Cooperative Laboratory of Traditional Chinese Medicine Modernization and Innovative Drug Development of Chinese Ministry of Education (MOE), College of Pharmacy, Jinan University, Guangzhou 510632, China

[⊥]Yunnan University of Traditional Chinese Medicine, Kunming, China

* To whom correspondence may be addressed. Corresponding to: Rong-Rong He, E-mail: rongronghe@jnu.edu.cn; Mingxian Liu, E-mail: liumx@jnu.edu.cn
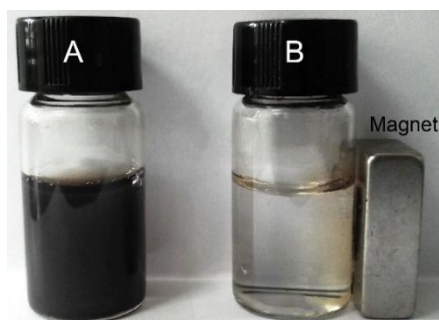
Figure S1. Digital photographs of HNTs@Fe$_3$O$_4$@PPy@DOX (A) without or (B) with magnets after 30 min dispersed in PBS.
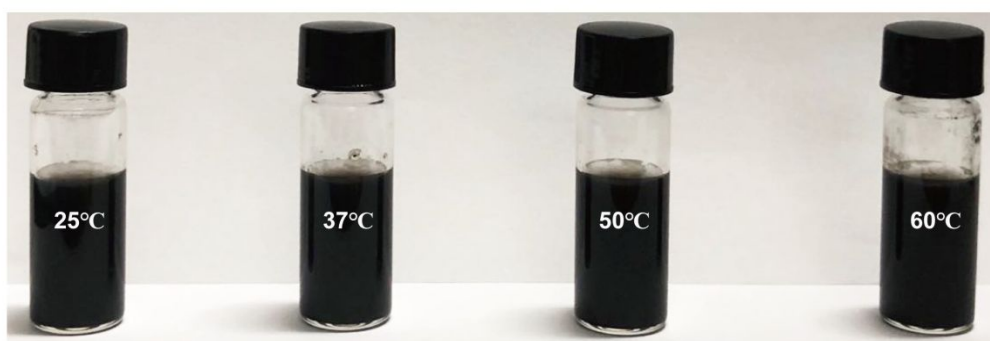

Figure S2. Digital photographs of HNTs@Fe$_3$O$_4$@PPy@DOX (1 mg/mL) dispersed in PBS at different temperatures (25, 37, 50, 60 °C) after 4 h.
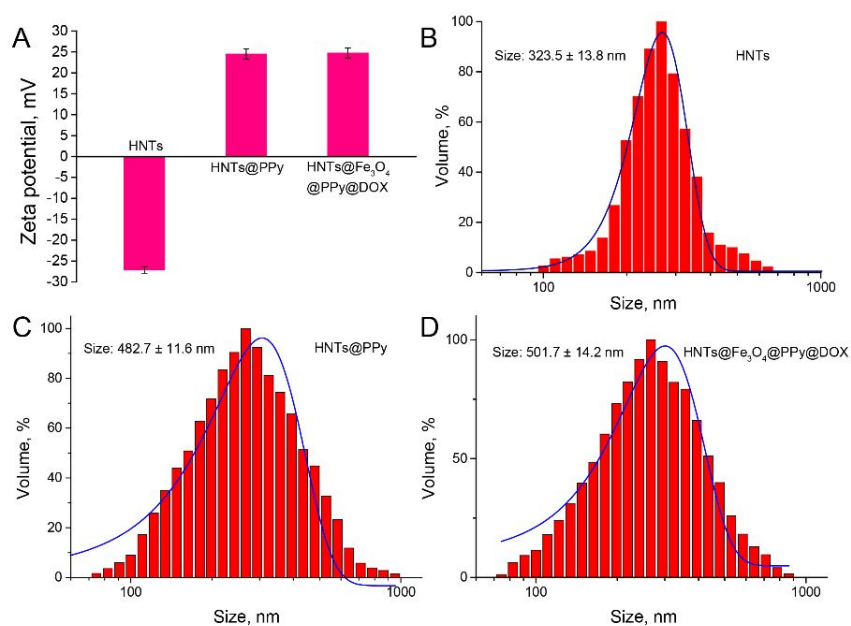

Figure S3. (A) Zeta potential data for HNTs, HNTs@PPy and HNTs@Fe$_3$O$_4$@PPy@DOX, (B-D) Particle size results of HNTs, HNTs@PPy and
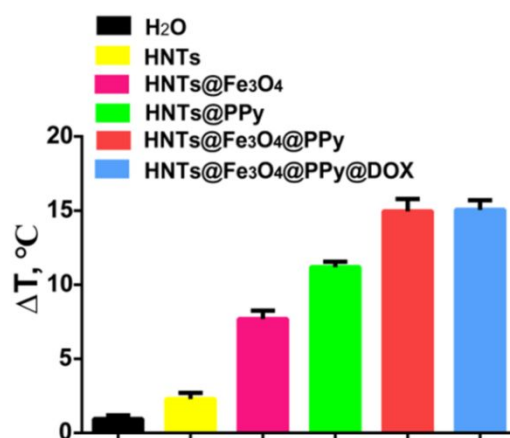
HNTs@Fe$_3$O$_4$@PPy@DOX.

Figure S4. Temperature increase of H$_2$O, HNTs, HNTs@Fe$_3$O$_4$, HNTs@PPy, HNTs@Fe$_3$O$_4$@PPy and HNTs@Fe$_3$O$_4$@PPy@DOX in the aqueous dispersion (1 mg/mL, 1 mL) irradiated by 808-nm laser (1 W/cm^2) after 5 min. The data are represented as mean ± SD (n = 3).
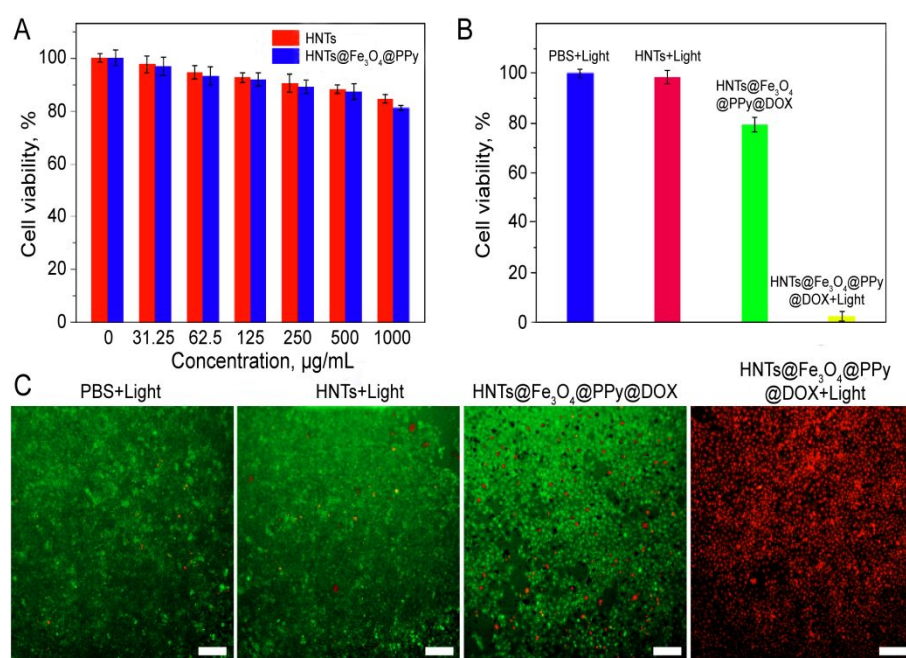

Figure S5. (A) Relative survival of 4T1 cells treated with different concentrations of HNTs and HNTs@Fe$_3$O$_4$@PPy for 24 h. (B) The relative survival rate of 4T1 cells incubated with HNTs and HNTs@Fe$_3$O$_4$@PPy@DOX for 12 h and then with or without irradiation (808 nm, 1 W/cm^2) for 8 min. The data showed mean ± SD (n = 4). (C) Fluorescent images of 4T1 cells incubated with HNTs and

HNTs@Fe$_3$O$_4$@PPy@DOX, with or without 808 nm laser (1 W/cm^2) irradiated for 8 min. Scale bar: 50 μm. The data are represented as mean ± SD (n = 3).
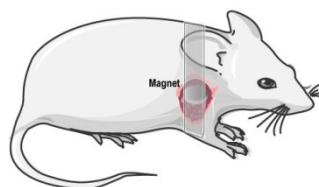

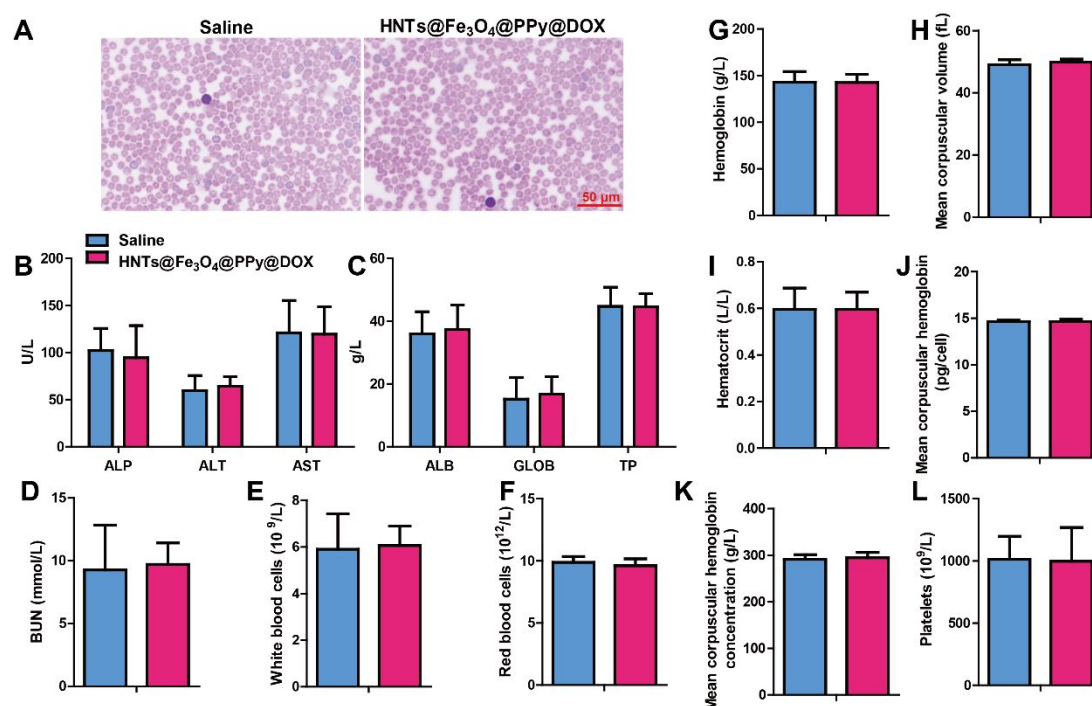**Figure S6.** Schematic diagram of a magnet-attached tumor-bearing mouse.

Figure S7. In vivo hemocompatibility and toxicity assay of HNTs@Fe$_3$O$_4$@PPy@DOX. (A) The blood smears photomicrographs of mice intravenously injected with normal saline, HNTs@Fe$_3$O$_4$@PPy@DOX. (B-D) Variety of biochemistry parameters including alkaline phosphatase (ALP), alanine aminotransferase (ALT), aspartate aminotransferase (AST), albumin (ALB), globulin (GLOB), total protein (TP), blood urea nitrogen (BUN). (E-L) Various hematology index including white blood cells, red blood cells, hemoglobin, mean corpuscular volume, hematocrit, mean corpuscular hemoglobin, mean corpuscular hemoglobin concentration and platelets. The values are represented as mean ± SD (n = 3), Scale bar: 50 μm.
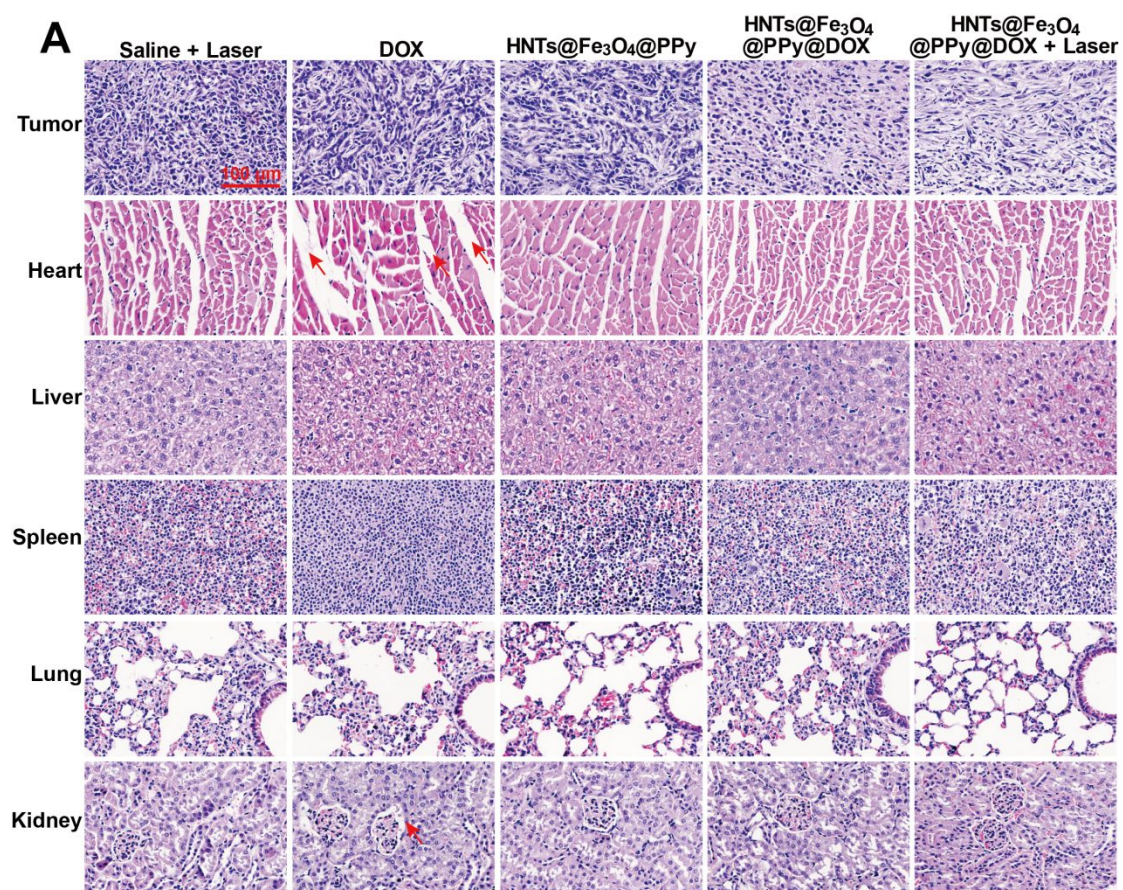
Figure S8. Histopathological analysis of HNTs@Fe$_3$O$_4$@PPy@DOX in 4T1-bearing mice. (A) H&E staining photographs of tumors and tissues harvested from various group at end of experiment. Scale bar: 100 μm. The red arrows in heart sections indicate the breakdown and dispersion of certain cardiomyocytes. The red arrow in kidney sections indicates the destructive necrosis of the glomerulus.